THESIS FOR THE DEGREE OF LICENTIATE OF ENGINEERING

Aqueous Organic Redox Flow Batteries

Electrochemical studies of quinonoid compounds

Cedrik Wiberg

Department of Chemistry and Chemical Engineering

CHALMERS UNIVERSITY OF TECHNOLOGY

Gothenburg, Sweden 2019

Aqueous Organic Redox Flow Batteries
Electrochemical Studies of Quinonoid Compounds
CEDRIK WIBERG

Department of Chemistry and Chemical Engineering
Chalmers University of Technology
SE-412 96 Gothenburg
Sweden
Telephone + 46 (0)31-772 1000

Cover:
Schematic of an aqueous organic redox flow battery employing quinones as redox-active materials.

Chalmers Digitaltryck
Gothenburg, Sweden 2019

Abstract

Society faces a large challenge in transitioning to sustainably generating electricity from renewable energy sources such as wind and solar. One of the biggest obstacles to this transition is the intermittence of the sources, leading to a mismatch of supply and demand, a problem most commonly solved by installing large-scale energy storage.

A promising energy storage technology that has the potential to surpass the currently used systems in performance, cost and environmental benignity are aqueous organic redox flow batteries (AqORFB). In this work, the performance of the archetypical AqORFB candidate, 9,10-anthraquinone-2,7-disulfonic acid (AQDS) is investigated by the novel combination of rotating disk electrode voltammetry and diffusion NMR. At a concentration of 1 mM, AQDS shows near ideal electrochemistry, involving two electrons, but at higher concentrations, the redox kinetics and the accessible charge/discharge capacity suffer. The former problem is examined by employing the scheme of squares model to explore the redox mechanism for AQDS at different pH values and is seen to come from rate-limitations in the protonation step. At higher concentrations, the relative concentration of protons to AQDS is lower, resulting in a larger impact on the rate-limiting step on the apparent rate constant. The latter is explained by self-association of the molecule into an electrochemically inactive dimer, and this process limits the capacity that can be collected from the system with bulk electrolysis. At a concentration of 1 M AQDS in 1 M H_2SO_4, only 27% of the molecules occur as redox-accessible monomers.

Furthermore, in pursuit of an attractive molecular candidate for AqORFBs, a naphthalene diimide molecule containing a solubilizing quaternary amine as a sidechain is synthesized and characterized both chemically and electrochemically. It is seen to show excellent behavior for AqORFBs by having a two-electron reduction at a suitable potential, a cheap and environmentally friendly synthesis route as well as showing exceptional stability during cycling with bulk electrolysis. The collection of cyclic voltammograms at a concentration of 1 mM over a range of different pH values revealed some interesting electrochemical behavior. Firstly, the reduction of only one of the two electrons shows any pH dependence, and only at pHs between 0 and 3. At pH 0, the two electrons share the same reduction potential, whereas at higher pH, they are separated by about 0.4 V. Secondly, at higher concentrations, this separation increases further, reaching 0.6 V at 50 mM, possible allowing for the molecule to be used as both anodic and cathodic material in a symmetric flow battery. Thirdly, the Potential - pH dependence between pH 0 and 3 exhibited a two electron-three proton relationship, possibly indicating self-association. Utilizing the same combination of diffusion NMR and rotating disk electrode voltammetry as for AQDS, the naphthalene-based molecule was found to dimerize similarly to AQDS, but to a larger extent. The capacity accessible for reduction using bulk electrolysis was close to the theoretical value, however, indicating no negative effect of the dimerization.

Acknowledgements

Funding from the Swedish Research Council as well as the Swedish Research Council FORMAS is acknowledged.

I am very thankful for the interesting research discussions and excellent supervision I have had with Professor Elisabet Ahlberg. If not for her expertise, this thesis would be long delayed and severely lacking. Professor Ergang Wang is acknowledged for gracefully giving me the opportunity to pursue this PhD.

I would also like to extend my thanks to my wonderful colleagues, Mariza, Petri, Kim, Ulises, Qunping, Christian and Isabelle for the social, emotional and institutional support throughout. The people I have shared the division of Applied Chemistry with also deserve special thanks, I look forward to two more years with you by my side. Thanks to Professor Jerker Mårtensson for being the examiner of this project, and to Professors Per Lincoln and Hanna Härelind for support in administrative and other tasks. Thanks to our administrator Lotta Pettersson for administering happiness and great working environment.

Heartfelt thanks to Francis Owusu for allowing me to supervise his Master Thesis, and his hard work with the naphthalene diimides. I am very happy with your results, and hope you enjoy reading this thesis.

Finally, thanks to my family and friends, for being helpful and supportive through thick and thin.

Contents

List of Publications

Paper 1. Dimerization of 9,10-Anthraquinone-2,7-Disulfonic Acid (AQDS) and its Impact on Aqueous Redox Flow Battery Performance

Cedrik Wiberg, Thomas J. Carney, Fikile Brushett, Elisabet Ahlberg, Ergang Wang*

Manuscript

Paper 2. Electrochemical Evaluation of Napthalene Diimide (NDI) for Aqueous Redox Flow Batteries

Cedrik Wiberg, Francis Owusu, Ergang Wang, Elisabet Ahlberg*

Manuscript

Contribution Report

Paper 1. All experimental work, data processing and writing the manuscript as first author.

Paper 2. Supervision of Francis, the master student who performed the synthesis, part of the chemical and electrochemical characterization; most electrochemical experimental work, the remaining part of the chemical characterization as well as writing of the manuscript as first author.

Abbreviations

RM	Redox-active Molecule
AQDS	9,10-Anthraquinone-2,7-disulfonic acid
NDI	Naphthalene Diimide
CV	Cyclic Voltammetry / Cyclic Voltammogram
RDE	Rotating Disk Electrode
BE	Bulk Electrolysis
NMR	Nuclear Magnetic Resonance
RFB	Redox Flow Battery
ORFB	Organic Redox Flow Battery
AqORFB	Aqueous Organic Redox Flow Battery

i_l	Diffusion-limited current (A)
n	Number of electrons
F	Faraday's constant (96485 C mol^{-1})
A	Geometric electrode area (cm^2)
C	Concentration (mol cm^{-3})
D	Diffusion coefficient (cm^2 s^{-1})
ω	Rotation rate (rpm)
v (Levich Equation)	Kinematic viscosity (cm^2 s^{-1})
v (Randles-Sevcik Equation)	Scan rate (V s^{-1})
i_p	Peak current (A)
R	Ideal gas constant (8.314 J mol^{-1} K^{-1})
T	Temperature (K)
Q	Reaction quotient

1 Introduction

Figure 1.1a shows the atmospheric carbon dioxide levels over the last two millennia, and Figure 1.1b shows the annual average global surface temperature relative to that between the years 1951-1980. As can be seen, the current global temperature anomaly is close to 1 °C, and 17 out of the 18 warmest years ever recorded have all occurred since 2001. Historically, the global temperature is known to have fluctuated significantly the last few hundreds of millions of years, and logically, the question arises whether the recent development is anthropologic or simply part of earth's natural climate cycling.[1, 2] The reasoning of a greenhouse effect, where gases, namely water and carbon dioxide in the atmosphere selectively absorb and block radiative heat from the sun was explored in the mid-nineteenth century by John Tyndall, but at that time it was believed that water was the most potent greenhouse gas.[3] In 1896, Svante Arrhenius released a comprehensive correspondence, carefully and methodically showing the great absorptive power of carbon dioxide and states that "I should certainly not have undertaken these tedious calculations if an extraordinary interest had not been connected with them". He closes the correspondence by showing that an increase of between 2.5 and 3 times in the contemporary carbon dioxide values would lead to a temperature increase of about 8-9 °C in the arctic regions and pointed out that the "combustion and decay of organic bodies" is a significant supply of carbonic dioxide to the atmosphere. That the concentration of carbon dioxide in the atmosphere is rising steeply, there is little doubt about. Since 1958, the carbon dioxide levels have increased by about 60%, with current global levels at almost 410 ppm, a level last seen more than 800 000 years ago.[4, 5]

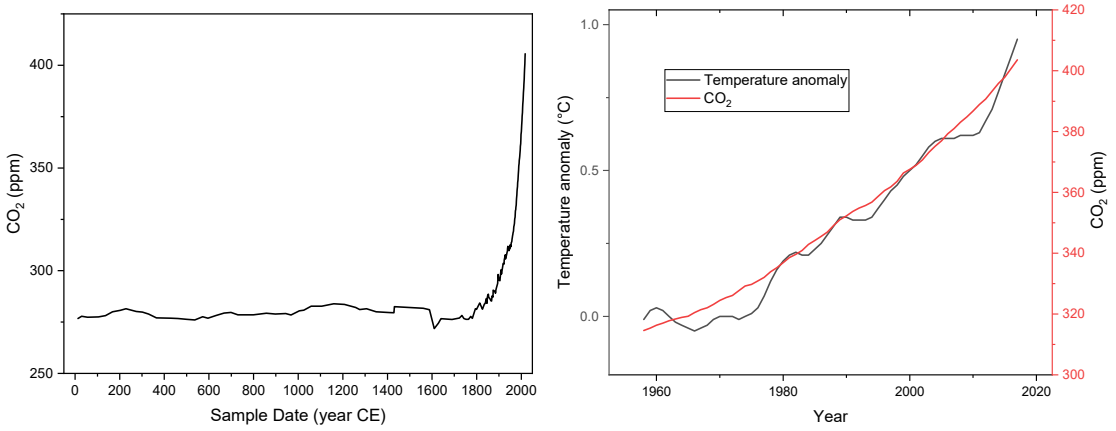

Figure 1.1: a) Merged plot of carbon dioxide levels. Year 0-1958 show data acquired from drilled ice cores,[6, 7] and 1958-2018 from the Mauna Loa observatory[5] and b) CO_2 data from the Mauna Loa observatory[5] and temperatures from NASA.[8]

As a consequence of the urgent need to reduce carbon dioxide emissions, a lot of effort is put into generating electricity from renewable energy sources such as hydropower, wind and solar, and as of the end of 2017, 26.5% of the global electricity was generated renewably.[9] Although 16.4% consisted of hydropower, the technology's installed power capacity value has only increased by about 30% the last decade, compared to the expansions of wind and solar, which have followed exponential trends since the end of the last century.[9-11]

One of the biggest hurdles to the transition from fossil-based energy sources to wind and solar is the intermittency of the sources; electricity is demanded regardless of whether the sun is shining, or the wind is blowing. To overcome this obstacle, large-scale energy storage systems need to be developed and deployed,[12-14] and the choice of technology needs to be made judiciously. Currently, about 96% of the global utility-scale energy storage comprises pumped hydroelectric energy storage and

about 2% electrochemical energy storage, such as lithium-ion batteries and redox flow batteries (RFB).[9]

If the transition from unsustainable electricity generation to renewables is to be made on a global scale, wind and solar power capacities will need to grow from the current level of 1 terawatts to roughly 10 terawatts.[9] It has been reported that green energy production alone can only meet 63% of the load without being supported by energy storage, due to solar and wind intermittency.[15] Hence, crudely approximating that 20% of the power output in this scenario, summing up to 2 terawatts, needs to be covered by battery storage, today's 158 GW storage power capacity needs to increase almost thirteenfold to meet the demand. Adding in the need for energy storage in other applications than renewable energy, it is clear that a gargantuan amount of energy storage will be needed and potentially deployed in the next few years or decades. In choosing which technology to dominate this new market segment, policy makers must account for other factors than cost/performance ratios, such as infrastructural impacts, environmental impacts as well as the safety of the energy storage technology.

1.1 Redox Flow Batteries

Redox flow batteries, sometimes referred to as regenerative fuel cells, consist of two separate tanks containing electrolyte solutions that are pumped through fuel cell-like reactors upon operation.[16] The electrolyte solutions are typically aqueous and contain redox-active molecules (RM) as well as a supporting electrolyte, often sulfuric acid.[17, 18] The solutions in the two tanks contain two different RMs, alternatively the same RM but at different oxidation states, and the difference in reduction potential between the two molecules determines the open-circuit voltage. The solution containing the molecule with the more negative redox potential is called the negative electrolyte, negolyte or catholyte, and the solution containing the molecule with the more positive redox potential is called positive electrolyte, posolyte or anolyte. The supporting electrolyte serves to make the solution ionically conductive and provide the system with mobile charge carriers.

During discharge, the electrolyte solutions are pumped through an electrochemical cell consisting of two porous electrodes, which are separated by an ion-selective membrane. The electrodes are typically graphite-based materials designed to have a large surface area and high mechanical stability,[19] whereas the choice of membrane will vary strongly depending on the electrolyte.[20-22] However, Nafion ion-exchange membranes are the most commonly used ones.[22] The molecule in the anolyte, once it reaches the surface of the porous electrode, gets oxidized and gives off an electron which is conducted through an external circuit and used as electricity. At the same time, the catholyte receives an electron from the porous electrode on the cathodic side, and thus gets reduced. Since an electron has effectively been transported from one side of the cell to the other, a charge imbalance has arisen. To negate this, a cation or a proton migrates through the membrane from the anodic to the cathodic chamber of the electrochemical cell. Figure 1.2 shows the operation of a quinone-based organic flow battery.

The capacity, in kWh, of a redox flow battery is determined by the amount of material dissolved in the solution, the amount of solution and the voltage. As such, capacity fade in redox flow batteries usually originates from chemical degradation of the RMs; especially in the case of organic flow batteries, and diffusion of the RMs through the membrane (crossover).[16, 23]

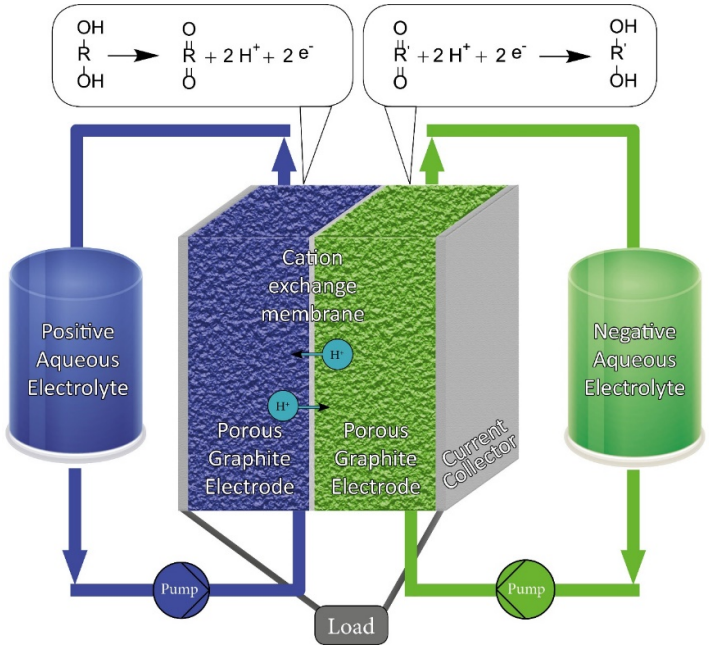

Figure 1.2: A schematic over a redox flow battery. In this case, a hydroquinone is oxidized to a quinone on the anode and a quinone is reduced to a hydroquinone on the cathode.

The setup with the redox-active material stored in tanks and the redox reaction occurring in cells that are separated from the tank means that the power and capacity of the system can be scaled independently. If more storage capacity (kWh) is desired, the tanks can be expanded and filled with more electrolyte solution. If, on the other hand, a higher power output (kW) is required, the size or number of the electrochemical cells can be increased, allowing for faster charge and discharge. This characteristic makes flow batteries well-suited for large-scale grid-connected energy storage applications, as the system can be tailored for the specific demands of each deployment. The modular design of the system also allows for easy maintenance or replacement of each component, which can be considered a large advantage over the currently used lithium ion batteries, which typically contain large amounts of aluminum, cobalt, lead and lithium that are seldom recycled.[24, 25]

Finally, the use of aqueous electrolytes makes the system inherently inflammable and less toxic, compared to $LiCoO_2$-based batteries. Upon heating beyond 120 °C, they are known to suffer from exothermic chain reactions due to the decomposition of the lithium cobalt oxide, a reaction that releases oxygen which can lead to severe fire and explosion hazards.[26, 27]

Current commercial redox flow systems include all-vanadium,[17] zinc-bromide,[28] and iron-chromium technologies,[29] with the vanadium-based setup having reached, by far, the highest level of market maturity among the three.[17, 28, 29] The all-vanadium redox flow battery was first successfully demonstrated in 1988 by Rychcik and Skyllas-Kazacos,[17] and routinely offers lifetimes in the range of 20 000 cycles due to the possibility to remix the two vanadium species in order to counteract the effect of RM crossover. As there is no chemical degradation of the vanadium species, the vanadium flow batteries suffer very small capacity fade over time. The biggest hurdle to their market penetration is the limited and volatile supply of vanadium.[30]

1.2 Organic Redox Flow Batteries

Organic flow batteries (ORFB) can be categorized by the solvent used; aqueous or non-aqueous.

1.2.1 Aqueous Organic Redox Flow Batteries

One of the most promising energy storage candidates to clear the aforementioned challenges of performance, cost and environmental sustainability are aqueous organic redox flow batteries (AqORFB).[12, 20, 31-35] Due to the possibility to tune the electronic properties of a molecule by chemical functionalization, a lot of work is being done on designing organic RMs with the desired properties. By adding groups that add polarity or charge to the molecule, the aqueous solubility can be increased, and by adding electron-donating or electron-withdrawing groups to the conjugated system, the reduction potential can be shifted to more negative or positive values respectively.[36, 37] Organic molecules also have the advantage that they benefit from large scale production, thus avoiding the material scarcity issues that vanadium flow batteries as well as lithium-ion batteries suffer from. In 2014, the seminal Nature paper by Huskinson, Marshak, Suh, Er, Gerhardt, Galvin, Chen, Aspuru-Guzik, Gordon and Aziz [18] reported a flow battery employing 9,10-anthraquinone-2,7-disulfonic acid (AQDS) on the negative side, and HBr on the positive side, displaying excellent performance in terms of cycling stability and energy efficiency.

Since then, numerous organic molecules, often quinones, have been considered for use in AqORFBs, with varying performance.[36-41] The design challenge is to find molecules that have reversible reductions with potentials close to either extremes of the electrochemical stability window of water. If the molecule has reduction potentials that are too negative or positive, the hydrogen evolution reaction (HER) or the oxygen reduction reaction (ORR) will take place instead of the reduction of the RM. Since the kinetics of the parasitic reactions are quite slow on graphite electrode surfaces, the range of the potentials can be extended slightly, indicated by the dashed lines in Figure 1.3.

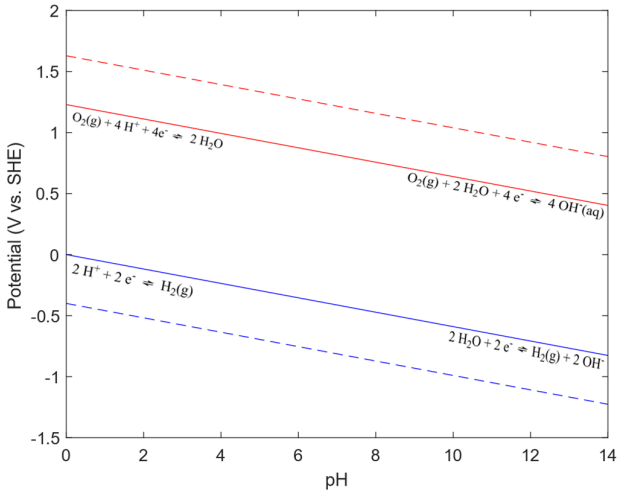

Figure 1.3: Pourbaix diagram of the electrolysis of water. The solid lines show the thermodynamic reduction potentials of the HER and ORR, and the dashed lines show that the range can be extended slightly for graphite electrodes due to sluggish kinetics.

Apart from having a suitable reduction potential, the molecule needs to have a high water solubility in the range of 1 M if it contributes with two electrons per molecule,[12, 33] it needs to have excellent chemical stability at all states of charge, be cheap, environmentally friendly to produce and non-toxic.

1.2.2 Non-Aqueous Flow Batteries

Non-aqueous flow batteries often employ acetonitrile, dimethyl carbonate, diethyl carbonate, propylene carbonate or a mixture of them as solvent. The choice of organic solvents opens up the

possibility to choose RMs with a wider range of reduction potentials, due to the wider electrochemical stability windows for organic solvents, with cell voltages upwards of 4 V being possible.[42] However, the advantage of a significantly higher cell voltage is balanced by the decreased electrical conductivity of the electrolyte, the use of expensive, often fluorinated supporting salts, decreased RM solubility in the solvent, flammability, solvent cost, and RM stability issues.[12, 42, 43] The stability issues are related to the fact that the use of organic solvents is only warranted when high voltages can be achieved, and an organic molecule with oxidation states very far apart in energy is likely to be more labile.

2 Aim and Scope

This doctoral project serves to examine whether it is possible to find high-performing materials for aqueous organic redox flow batteries (ORFB) by modifying materials that have a current use in non-aqueous ORFB or polymer solar cells into water soluble molecules by functionalization with quaternary amines or sulfonic acid groups.

Additionally, the aim is to see whether there are - for the aqueous ORFB research community - helpful pieces of knowledge to be obtained by doing deeper electrochemical analyses on the mechanistical electrochemical behavior of organic molecules in aqueous electrolytes. In this context, the extent and consequence of RM dimerization on flow battery performance is a topic of particular attention.

3 Methods

In the initial stages of the project, an electrochemical evaluation of the archetypical aqueous organic flow battery molecule, AQDS, was done. It has been reported, that the molecule seems to self-associate into a dimeric structure at higher concentrations, and as a consequence of this, it was seen that the accessible capacity by cyclic voltammetry (CV) and bulk electrolysis (BE) was reduced significantly.[44] To shed light on this behavior, AQDS was characterized chemically and electrochemically, at a set of concentrations ranging from 1-250 mM, using CV, rotating disk electrode (RDE) voltammetry together with diffusion NMR. The evaluations were performed in a 1 M pH 9.76 sodium carbonate buffer, referred to as “Buffer”, and a 1 M H_2SO_4 solution, referred to as “Acid”. The results from this work are presented in Paper 1.

In parallel, organic synthesis was employed to produce suitable candidate molecules. Naphthalene diimide (NDI), a molecule that has been used in polymer solar cells and organic thin-film transistors, was synthesized with quaternary amine sidechains. This was made under the assumption that its electronic properties and exceptional stability which made it a popular choice in the solar cell field could be transferred into aqueous flow battery applications.[45, 46] The molecule was evaluated for its suitability in AqORFBs by CV, RDE, ^{1}H-NMR, diffusion NMR and BE, resulting in Paper 2.

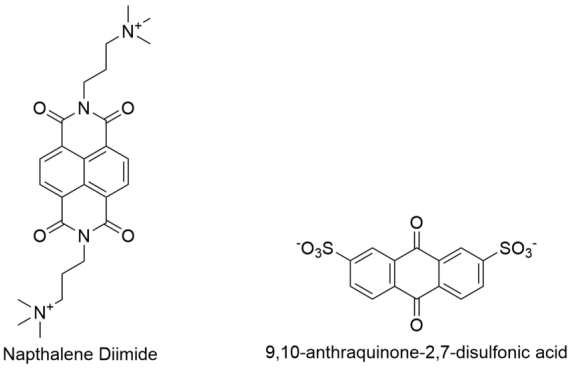

Figure 3.1: Chemical structures of the molecules examined in the present work.

4 Theory

4.1 Cyclic Voltammetry and Rotating Disk Electrode Voltammetry

Cyclic voltammetry (CV) is arguably the electrochemist's most commonly used analytical tool to electrochemically characterize a molecule or system. It is a comparably simple method to set up, and a wealth of information can be obtained, if performed and interpreted properly.[47] In some cases, CV can be complemented with rotating disk electrode (RDE) voltammetry in order to acquire additional information about the system, often related to diffusion and kinetics.[48, 49] For both methods, as well as in most other electrochemical systems, the setup comprises a working electrode, a counter electrode and a reference electrode.[50] The surface of the working electrode is where the redox reaction of interest takes place. But any electron moving into or out of the working electrode means another electrode needs to do the opposite operation at the counter electrode. The reference electrode serves to give the system a constant potential to which the potential of the redox reaction can be related. In RDE, the working electrode is rotated at a set of different rates, which provides the electrode surface with a steady stream of new material, the amount of which depend on the rotation rate.

Figure 4.1 shows a CV and RDE scan for 1 mM AQDS in a slightly alkaline sodium carbonate buffer solution. This system behaves ideally and serves as a good model system. Beginning at a more positive potential than what is required to reduce the molecule, the bias is swept linearly with a set sweep rate. Eventually, when reaching a sufficiently negative potential, the material starts reducing, generating a negative current. Once molecules at the electrode surface begin to reduce, a concentration difference is established against the bulk concentration. Thus, unreduced material will start diffusing from the bulk solution towards the electrode surface according to Fick's law of diffusion.[51] Continuing in the negative direction, the reduction current increases until the current reaches a maximum, signifying that the rate of reduction has surpassed the rate of diffusion, and that the concentration of active material at the electrode surface at this point is zero.

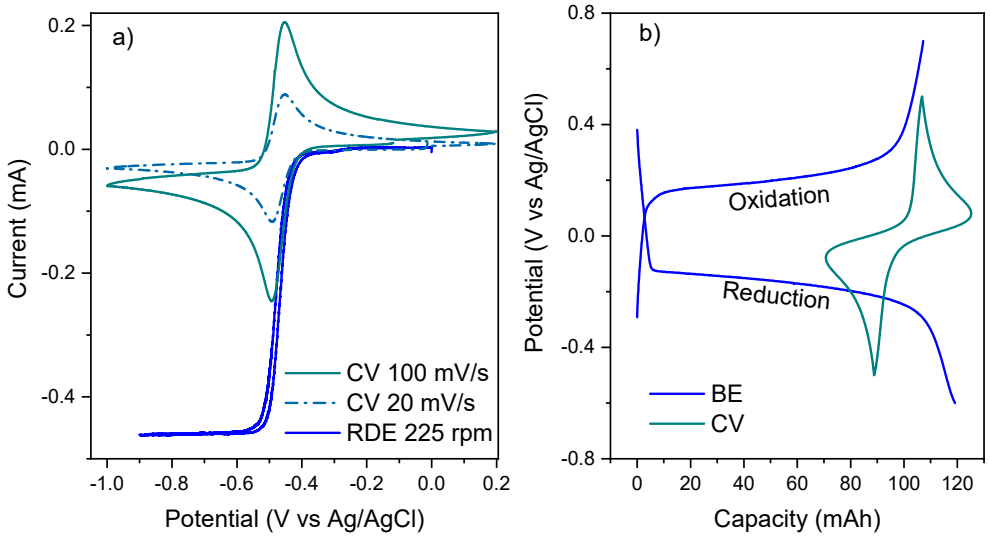

Figure 4.1: a) CVs and RDE of 1 mM AQDS in pH 9.76 sodium carbonate buffer, b) BE and CV of 50 mM AQDS in 1 M H_2SO_4.

For the CV case, if a faster sweep rate is used, the active material at the surface is depleted more quickly, resulting in a larger concentration gradient being formed, which in turn yields higher peak maxima. The peak height is thus a measure of the concentration and diffusivity of the active species, which is seen in the Randles-Sevcik equation for a reversible electron transfer reaction:[51-53]

$$i_p = 0.4463nFAC\left(\frac{nF\nu D}{RT}\right)^{\frac{1}{2}}, \qquad 1$$

where i_p is the peak current, n the number of electrons, F is Faraday's constant, A the electrode area, C the concentration, v the sweep rate, D the diffusion coefficient, R the gas constant and T the temperature.

Continuing past the maximum, the current decays as the concentration gradient between the surface and the bulk solution decreases, thereby lowering diffusion rate of unreduced material. After the last reduction reaction of interest has run its course, the direction of the sweep is reversed, and the reduced species are oxidized back, unless they have taken part in some external electrochemical or chemical reaction during the time passed since they were reduced. The peak to peak potential separation between the reduction peak and the returning oxidation peak can give information regarding the number of electrons and the electron transfer rate constant.

In the RDE case, the rotation rate determines the rate at which new material is transported to the surface, and typically, a large enough solution volume is used that the decrease in bulk solution is negligible. The result of this is that the current does not decay, as in the CV case, but instead reaches a plateau, which is termed the *diffusion-limited*, or *limiting current*, and relates to the diffusivity of the molecule, D, as well as the number of electrons, n, concentration, C, rotation rate, ω and kinematic viscosity, v, according to the Levich Equation:[51, 53]

$$i_l = 0.201nFA_{rde}CD^{\frac{2}{3}}\omega^{\frac{1}{2}}\nu^{-\frac{1}{6}}, \qquad 2$$

The returning sweep in the RDE case should overlap with the forward sweep, since it is a steady-state technique. In practice, however, a small hysteresis is often seen, due to, amongst others, blockage of the electrode surface, material depletion or capacitance.

4.2 Bulk Electrolysis

The bulk electrolysis (BE) cell consists of the same three-electrode setup as CV and RDE, but with the addition that the solution is stirred, the working electrode has a much larger surface area and is separated from the counter electrode by a membrane. The BE is run either potentiostatically, where the potential is fixed and the current response is measured, or galvanostatically, where the current is fixed and the potential is instead allowed to vary. Both methods have the same result; the bulk of the material in solution gets reduced or oxidized. A typical BE curve is shown in Figure 4.1b, where 80 ml of 50 mM AQDS in 1 M H_2SO_4 is reduced and then oxidized. As material is consumed in the process, higher and higher potentials are needed, due to the shifting of the reaction quotient *Q*, which relates to the reduction potential through the Nernst equation:[51, 53]

$$E_{cell} = E^0 + \frac{RT}{nF} lnQ. \qquad 3$$

For reactions involving protons, and once a conversion from the natural logarithm to the decadal logarithm is made, the following variation of Equation 3 uncovers:

$$E_{cell} = E^0 + \frac{0.059}{n} log[H^+] + \frac{RT}{nF} ln\frac{[R]}{[O]} = E^0 - \frac{0.059}{n} pH + \frac{RT}{nF} ln\frac{[R]}{[O]}, \qquad 4$$

where [R] and [O] are the concentrations of the reduced and oxidized species respectively.

The perhaps most important piece of information obtained from BE measurements is regarding the stability of the material. If the material can be reduced and oxidized through multiple cycles while yielding the same amount of charge every cycle, it can be considered stable, depending on the number of cycles.

4.3 Coupled Electron Transfers and Scheme of Squares

The following section covers some of the theory regarding electron transfer in a mathematically spartan manner. The reader is encouraged to consult Bard and Faulkner [51] or Compton and Banks [53] for the mathematical treatment of these concepts.

In the most general redox reaction scheme,

$$O + e^- \rightleftharpoons R, \qquad R1$$

a reactant O acquires an electron and is reversibly reduced to a product R. Depending on the relative energy levels – or potentials – of O, e^-, and R, there will exist one point in this equilibrium that is the most thermodynamically favorable one.[53] Any deviation from this point (which is characterized by the relative concentrations of O and R) will incur a difference in potential between the populations of the reactants and the products, according to Le Chatelier's principle.[53] In response to this, a redox reaction will occur, where electrons flow from the side that has the higher energy to the one with lower energy. In summary, the advance or retreat of R1 is governed by the relative abundances of O and R. This necessitates the electrochemist to take several different scenarios into account, where the concentrations of the reactants and products of a reaction are affected by external processes. The processes acting on the system can be categorized into being either an electron transfer reaction, denoted by the letter E, or a chemical reaction, C. Only a selection of all the possible situations will be covered in this section.

If prior to the above reaction, O is generated by a separate chemical reaction:

$$Y \rightleftharpoons O, \qquad R2$$

$$O + e^- \rightleftharpoons R \qquad R1$$

then the coupled reactions are termed to be of a CE type.[51] This is often applicable for the reduction of quinones in sufficiently acidic media, in which case the "C" is a protonation reaction.[54] If C is a protonation reaction, the forward reaction would be promoted by lowering the pH of the electrolyte solution, seen by a more positive reduction potential in accordance with Equation 4. Furthermore, if a CV is recorded, the relationship between the peak heights of the reductive and oxidative peak might be smaller than unity. This happens if the reactant continues to be generated close to the electrode surface, which will happen when the product of R2 is consumed in R1, which in turn pushes the equilibrium in R2 "to the left".

Similar to the separate reaction in which O was generated, there can exist reactions that instead consume R, leading to the following scheme this case, termed "EC":

$O + e^- \rightleftharpoons R$ R1

$R \rightleftharpoons X$ R3

How this appears in a CV depends on the reduction potential of species X. If X is not redox-active in the applied potential range, the peak from the oxidation of R back to O will be smaller than the reduction, depending on the equilibrium constant for reaction R3. If X has a reduction potential that is more positive than R, a second electron transfer will follow the C step, resulting in an ECE reaction. On the returning sweep of this ECE reaction, a two-electron oxidation will take place close to the reduction potential of X (assuming the product is stable and does not undergo any further reactions).[51]

Any combination of E's and C's is possible, and the character convention of E and C gives very compact abbreviations to possibly quite complex reactions. Depending on the pH, the reduction of a quinone can either involve two electrons, two electrons and one proton, or two electrons and two protons, largely determined by the pKa values of each formed species.[51, 55] As such, taking the order of the electron transfers and chemical reactions into account, nine different combinations are possible, which is depicted in a model called the *Scheme of Squares, see* Figure 4.2.

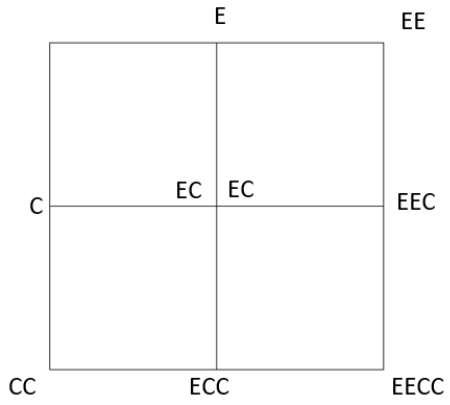

Figure 4.2: A general Scheme of Squares model for a system of two electron transfers (E) and two chemical reactions (C).

The pathway taken will be decided by relative rates between the competing reactions in each point, and thus, often not only one of the paths are taken. Furthermore, the path from the starting material to the product is not necessarily the same as the return route.[56]

Although the scheme of squares here is written for any combination of electron transfers and chemical reactions, it is most commonly applied to systems of coupled electron and proton transfers.[54-56]

4.4 Characterization of NDI Self-Association with ^{1}H-NMR

If not explicitly referenced otherwise, all of the following theory regarding Nuclear Magnetic Resonance (NMR) Imaging, and diffusion NMR is referenced to the comprehensive article by Price.[57]

NMR is one of the most commonly used tools at the chemist's disposal, with hydrogen being the nucleus most commonly utilized. When introducing the most abundant isotope of hydrogen, ^{1}H into a magnetic field, the nucleus will start *precessing*, the movement created by any spinning mass exposed to a gravitational force, for instance a spinning top. The frequency of the precession is proportional to the strength of the magnetic field. The reason why hydrogen, together with a few other nuclei precess in magnetic fields is because they have *non-zero magnetic spin moments.* For example, in a magnetic field of 9.6 Tesla, a ^{1}H nucleus will precess with a frequency of approximately 500.13 MHz, which is usually the figure of performance for a given magnet in an NMR system, as opposed to the actual field strength. This frequency is known as the Larmor frequency, ν_0, given by the Larmor equation:

$$\nu_0 = -\frac{\gamma B_0}{2\pi}, \qquad 5$$

where γ is the gyromagnetic ratio and B_0 the magnetic field strength. Hydrogen has a very high gyromagnetic ratio, making it sensitive to changes in the magnetic field, and thus popular for use in NMR analysis.

In the case of self-association, ^{1}H-NMR spectra of the analyte will show a concentration-dependent displacement of the chemical shift.[58, 59] The measured shift is an average between the shift of the monomer and the dimer due to the fast proton exchange between the monomer and the dimer,[60] exemplified in Figure 4.3.

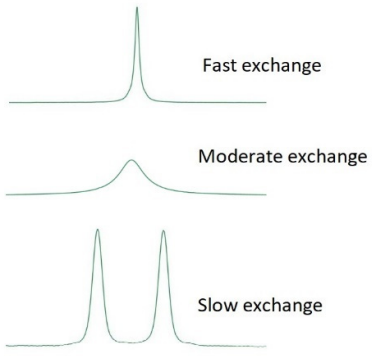

Figure 4.3: A depiction of the influence of exchange on chemical shift and peak shape.

The merged peak will have a concentration-averaged shift of the individual constituents, and modelled through the following equations:[44, 61]

Assuming only dimer formation – the dimer model:

$$\delta_{measured} = \delta_m + (\delta_d - \delta_m)\frac{\sqrt{1+8KC_0}-1}{\sqrt{1+8KC_0}+1} \qquad 6$$

Allowing higher order aggregates – the isodesmic model:

$$\delta_{measured} = \delta_m + \frac{4(\delta_d - \delta_m)KC_0\left(2 - \frac{4KC_0}{(1+\sqrt{1+4KC_0})^2}\right)}{\left(1+\sqrt{1+4KC_0}\right)^2} \qquad 7$$

Where δ is the chemical shift for the respective index, where d stands for dimer and m for monomer, K the equilibrium constant, and C_0 the total concentration. Although there are three unknowns, making an accurate curve fitting problematic, a good approximation of the monomer shift can sometimes be gained by measuring at low enough concentrations.

4.5 Diffusion NMR

In diffusion NMR, the sensitivity of the nucleus to changes in the magnetic field is taken advantage of by the application of a magnetic field gradient. When a gradient is applied, the nuclei located in the stronger part of the field will precess with a higher frequency than those subjected to a weaker field. In other words, this allows for spatial labelling of the nuclei based on their *precession* frequencies.

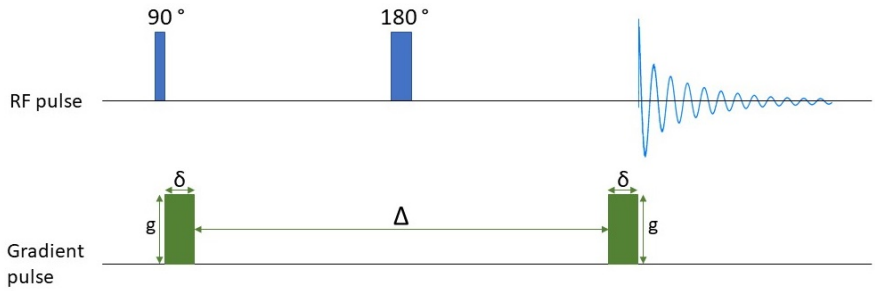

Figure 4.4: A typical pulse field gradient stimulated echo (PFGSE) pulse sequence.[57]

An example pulse sequence for measuring the diffusion of a sample is shown in Figure 4.4, although in practice, the commonly used sequences are more complicated.[57] A radiofrequency pulse (RF) is applied, perpendicular to the magnetic field, and the strength (g) and duration (δ) of the pulse is chosen so that the angle of the precession is shifted 90° away from the z-axis resulting in a xy-component of the precession. A magnetic gradient pulse of a certain strength and duration is then applied, *spatially encoding* the nuclei in the sample. Due to the difference in location of the nuclei, some will precess slightly more slowly than others leading in a decay in the signal. This is allowed for a time (Δ), during which the molecules self-diffuse. A 180° RF pulse is applied after half of Δ, flipping the spin of the nuclei, putting the more slowly precessing nuclei ahead of those precessing more quickly. In the absence of diffusion, this would lead to all the nuclei regathering at the end of Δ, resulting in what is called a spin-echo. However, due to the change in location during Δ, due to molecular self-diffusion, the regathering will be incomplete, and the spin-echo will be attenuated. This attenuation in peak height or integral, S, correlates to the diffusion coefficient of the analyte through the following equation:[57]

$$\frac{S}{S_0} = e^{-\gamma^2\delta^2 g^2 D(\Delta - \frac{\delta}{3})}. \qquad 8$$

5 Results and Discussion

The findings related to AQDS are presented first, followed by the characterization and evaluation of NDI. Excepting Figure 5.2, all figures, tables and numbers relating to AQDS are referenced to Paper 1. Figures, tables and numbers relating to NDI, are referenced to Paper 2.

5.1 AQDS

At the beginning of the AQDS project, it was suggested by Carney *et al.*[44] that AQDS, at higher concentrations, forms a dimer of some kind, and that the dimer could accept three electrons per dimer, as opposed to the ideal two electrons per monomer, which is seen at concentrations around 1 mM.

5.1.1 RDE and Diffusion NMR

The Potential – Current curves from the RDE voltammetry for 1 and 50 mM AQDS in acid and buffer are shown in Figure 5.1.

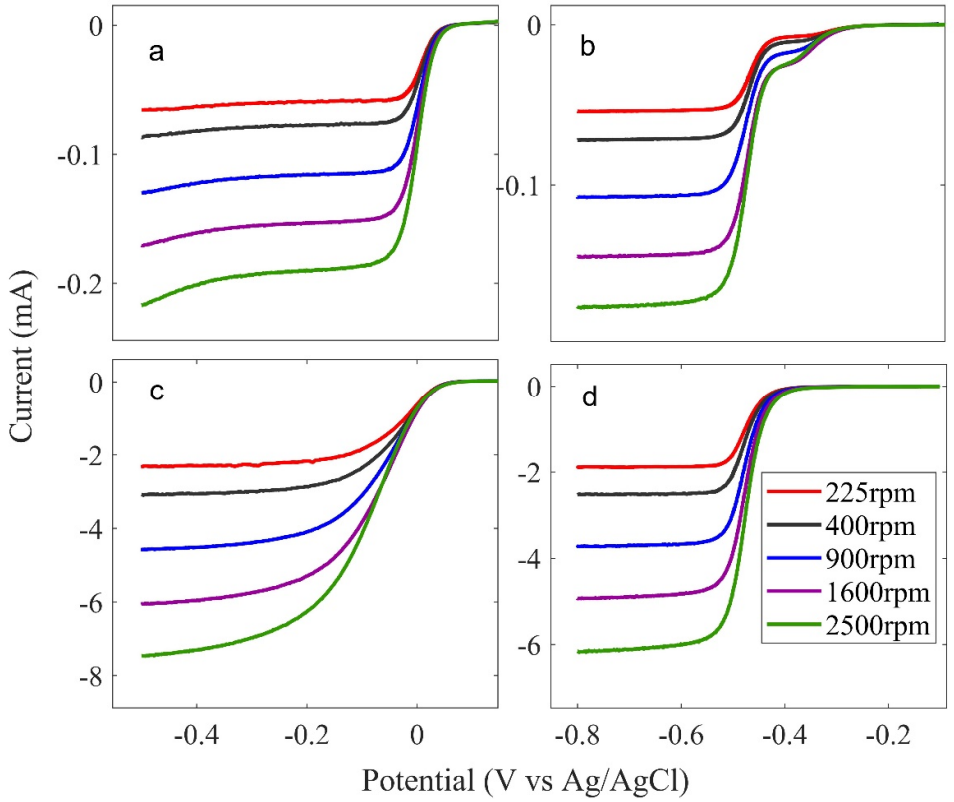

Figure 5.1: RDE voltammograms. The negative-going sweep is shown for a) 1 mM AQDS in acid, b) 1 mM AQDS in buffer, c) 50 mM AQDS in acid and d) 50 mM AQDS in buffer. Scan rate: 10 mV/s.

Upon analysis of the RDE results, it was seen that the diffusion-limiting currents, which are supposed to scale linearly with concentration according to the Levich Equation, see Equation 2, instead showed a polynomially decaying trend, see Figure 5.2. Additionally, at higher concentrations, especially in acid, a decrease in electrochemical reversibility, i.e. the kinetics, was seen, indicated by the elongated curve in Figure 5.2a compared to c.

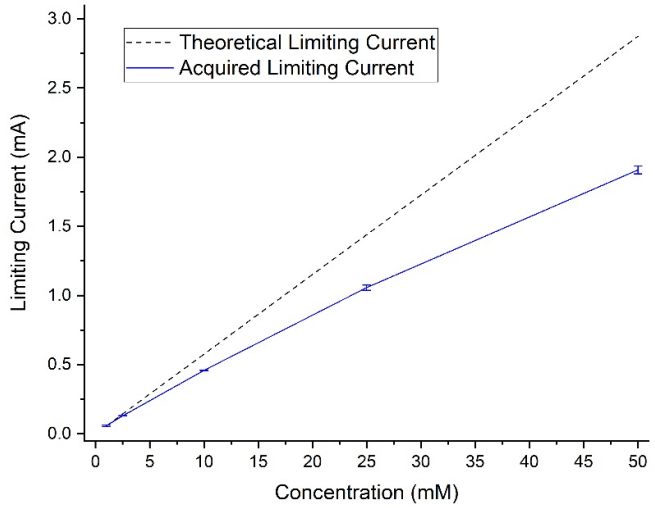

Figure 5.2: Limiting Current plotted against nominal concentration. The acquired limiting currents (solid blue line) show a clear deviation from the theoretical values (dashed lined).

According to the Levich equation, the low limiting currents could reasonably be explained by either a decrease in diffusion coefficient or in accessible concentration.

A shoulder can be seen in Figure 5.1b, which seems to originate from the reduction of adsorbed or surface-bound AQDS,[62] since it does not scale with concentration, and only scales with rotation rate until it reaches a current of about -0.03 mA. Due to the limited amount of the adsorbed species, the limiting currents are not affected, and the cause for the behavior was considered outside the scope of the work.

It was decided that it would be beneficial to acquire the diffusion coefficient from a non-electrochemical technique, namely diffusion NMR, and enter it into the Levich equation. Due to near-ideal behavior of AQDS at 1 mM, the dimerization at that concentration was considered negligible. Thus, the diffusion coefficients acquired for 1 mM of the solutions from NMR, which matched those acquired by RDE, were designated the "monomer diffusion coefficients" and found to be 3.8×10^{-6} $cm^2\ s^{-1}$ for both the acid and buffer solutions. A hypothesis was formed that the AQDS dimer is not redox-active within the aqueous electrochemical stability window, and that the Levich equation would yield the monomer concentration, if the monomer diffusion coefficient was inserted at the different concentrations. In effect, the Levich equation should not include any dependence on the dimer concentration. This operation yielded a set of accessible concentrations which are shown in Table 5.1.

Table 5.1: The redox-accessible concentrations of AQDS, as determined by coupling diffusion NMR and RDE.

Nominal conc. (mM)	1	2.5	10	25	50
Accessible conc. in acid (mM)	1.0 ± 0.0	2.6 ± 0.1	8.7 ± 0.1	20.2 ± 0.5	38.2 ± 0.4
Accessible conc. in buffer (mM)	1.0 ± 0.1	2.2 ± 0.0	7.7 ± 0.1	17.8 ± 0.3	32.2 ± 0.6

As can be seen, the decrease in accessible concentration already at 50 mM is significant. In order to test whether these accessible concentrations corresponded to a monomer concentration determined by the dimerization of AQDS, they were compared to those calculated by utilizing the equilibrium constant of 5 M^{-1} previously reported for the dimerization process of AQDS, which was acquired by

^{1}H-NMR.[44] As shown by the red lines in Figure 5.3, the accessible concentration corresponded well to the calculated equilibrium concentration of monomer, thus proving that the dimer is not possible to reduce under aqueous operating conditions. This result is the main finding of the AQDS work.

An equilibrium constant was fitted to the accessible concentrations in buffer as well, and was found to be 8 M^{-1}, indicating a stronger self-association than in the acid electrolyte.

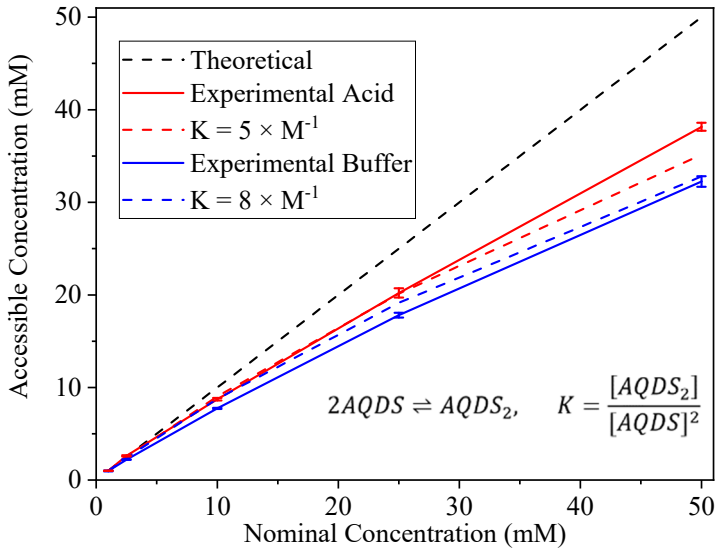

Figure 5.3: Comparison of the redox-accessible concentrations in Table 5.1 with those yielded by equilibrium constant of 5 M^{-1} and 8 M^{-1} for the acid and buffered cases respectively.

5.1.2 Cyclic Voltammetry

To support this result, cyclic voltammetry was employed. It was considered an advantage to show the same behavior with two separate techniques, and besides, with CV, higher concentrations could be investigated. The peak heights of a CV, in the absence of external effects, increase linearly with concentration, according to Randles-Sevcik equation, see Equation 1. However, looking at the CVs in Figure 5.4, the peak heights decrease with concentration, despite being normalized by the concentration.

The decrease in reversibility for the acid electrolyte can also clearly be seen in Figure 5.4a by the peak-broadening and increase of peak-to-peak separation. The decrease in reversibility leads to a deviation from the Randles-Sevcik equation, and thus, only the CVs in buffer were used for this experiment.

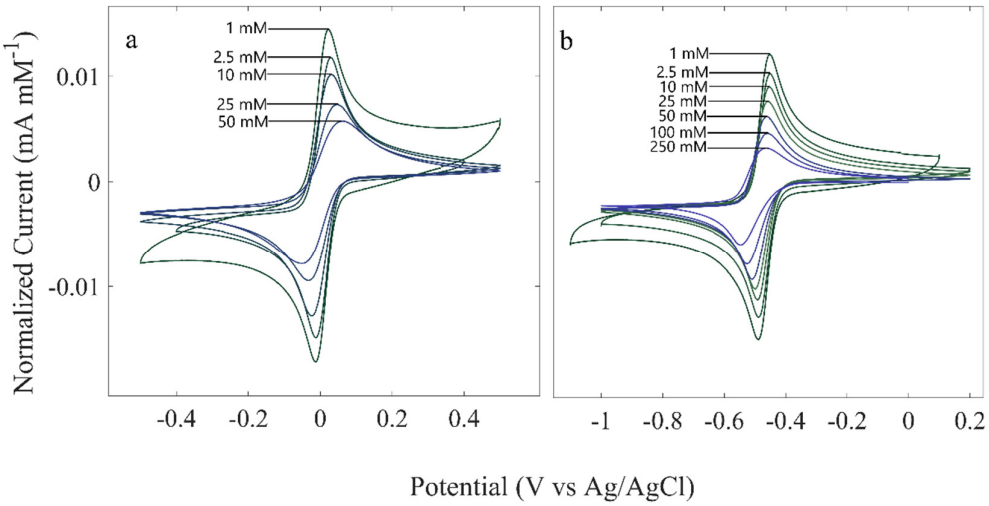

Figure 5.4: CVs of AQDS at varying concentrations in the a) acidic and b) buffered electrolyte. Scan rate 20 mV s^{-1}.

The decrease in peak heights yielded a set of concentrations that related admirably to those found in the RDE measurements. It was also seen that the dimerization dynamics were followed even at the high concentration of 250 mM, leaving little doubt about the redox-inactivity of the AQDS dimer.

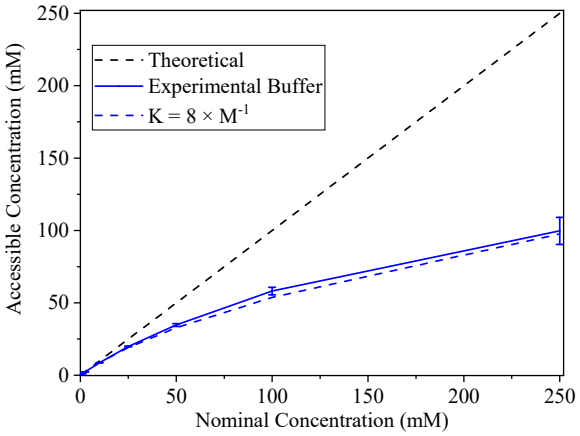

Figure 5.5: Redox-accessible concentrations obtained from the decreasing peak heights of CVs, solid blue line, and the monomer concentrations according to an equilibrium constant of 8 M^{-1}, dashed blue line.

It was hypothesized that whichever intermolecular interaction caused the dimerization of AQDS was temperature dependent and might be possible to eliminate by increasing the temperature of the system. Viscosity-normalized CVs of 100 mM AQDS in buffer at different temperatures are shown in Figure 5.6. The reductive peak height of AQDS at 100 mM at room temperature is 72% lower than expected by the Randles-Sevcik equation. The complete negation of the dimerization would thus result in an increased peak height corresponding to this number. This was, however, not seen, and it was concluded that although the dimerization might be partially counteracted by increasing the temperature, this did not solve the problem.

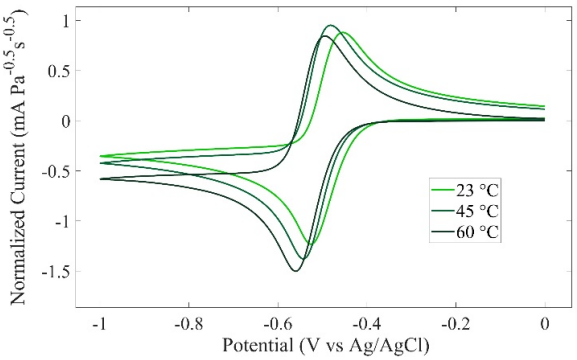

Figure 5.6: Viscosity-normalized CVs of 100 mM AQDS in buffer at varying concentrations. Scan rate: 50 mV/s.

5.1.3 Scheme of Squares Analysis of AQDS

The slower kinetics at higher concentrations were, however, to this point not yet addressed. To shed light on this phenomenon, the scheme of squares model was employed. Figure 5.7a shows the different possible reduction and protonation pathways for AQDS, including literature values of reduction potentials and pKa values. The values in parentheses[55] are given for 2,6-AQDS, which is assumed to behave similar to 2,7-AQDS, which is shown by comparing the pKa values of 2,7-AQDS of 10.6 and 7.6 to the 10.5 and 7.6 for 2,6-AQDS. Apart from that, Figure 5.4 shows reduction potentials conforming to those in Figure 5.7.

A detailed summary of the AQDS behavior according to the scheme of squares is given in Paper 1. Figure 5.7a shows the oxidation and protonation state for AQDS depending on the pH and applied potential. Figure 5.7b and c show the pathways for reduction and oxidation of AQDS at pH 0 and 9.76 respectively. Comparing the pathways for the different pHs, the main difference is that in acid, protonation needs to occur before electron transfer, due to the more positive reduction potentials of the protonated species compared to those of the deprotonated ones. Since a significant concentration-dependent kinetic impediment is seen only in acidic electrolytes, it is thus assumed that the proton transfer is rate-determining, and that the proton concentration in relationship to the concentration of AQDS will determine the kinetics in acid. The oxidative “return” route, on the other hand, has minimal proton dependence.

For the route in the buffered alkaline electrolyte, after the last reductive step, about 85% of the species get protonated, corresponding to pKa of 10.6 in pH 9.8. In the oxidative direction, unless the potential is directly stepped from the value of E_2 = -0.56 V to E_4= -0.13 V, the protonated population needs to lose the proton before oxidation. Seen on the unchanging potential of the oxidation peak for AQDS in the buffer in Figure 5.4b, the kinetics does not seem to suffer at increased concentrations. Therefore, it is assumed that the deprotonation is faster than the oxidation and does not limit the rate.

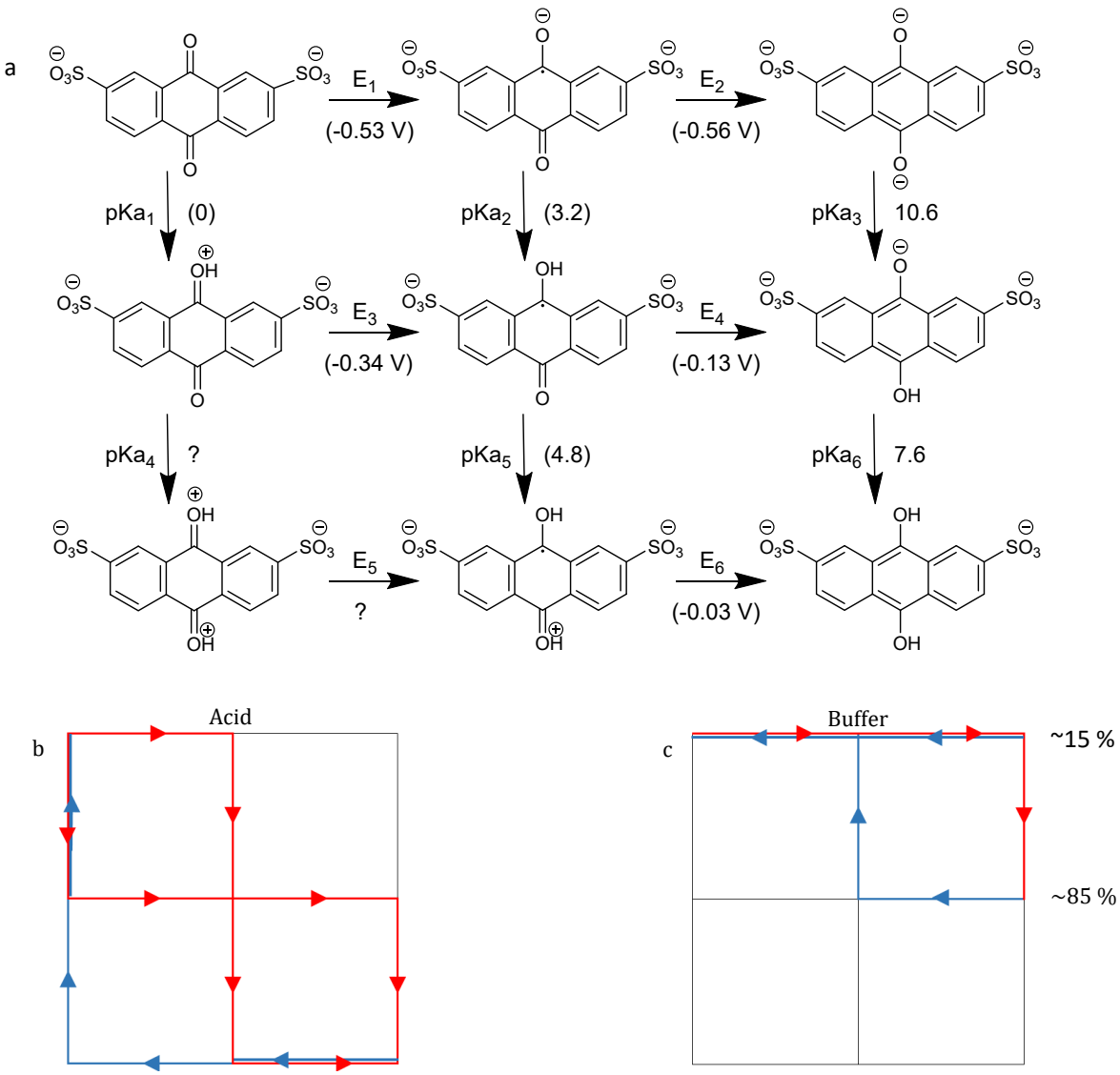

Figure 5.7: a) The scheme of squares for AQDS, showing the reduction/oxidation pathway depending on pKa and reduction potentials. Values in parentheses are taken for 2,6-AQDS and are assumed to be equal to those of 2,7-AQDS.[55] The values without parentheses were reported by Forster and O'Kelly [63]. b) and c) show the pathways for AQDS in the acid and buffer electrolytes respectively.

5.2 NDI

Similar to AQDS,[44] NDI has been reported to self-associate strongly in aqueous solutions, quantified by an equilibrium constant of K = 251 M^{-1} which was acquired by measuring ^{1}H-NMR spectra at a range of concentrations of NDI in D_2O.

The NDI molecule was synthesized in 70 g scale according to Figure 5.8 in a facile and manner with high yields and water as the only byproduct.

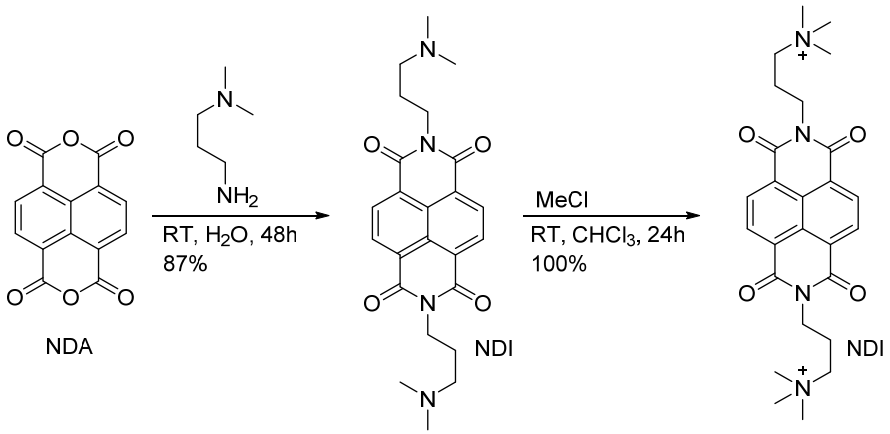

Figure 5.8: Synthesis procedure for the NDI used in this work.

The first step was done according to literature,[64] and the quaternization simply by bubbling chloromethane through a chloroform solution of the tertiary NDI, whereupon the pure product is precipitated. The last step was only done with a small fraction of the product from the first step and is only necessary if the molecule is to be examined at higher pH values. The tertiary amine sidechains are protonated for pH values less than about 8 (pKa ≈ 8.1) as shown by the titration curve in Figure 5.9. For actual flow battery applications, the last reaction step is thus possible to omit, making the synthesis quite green.

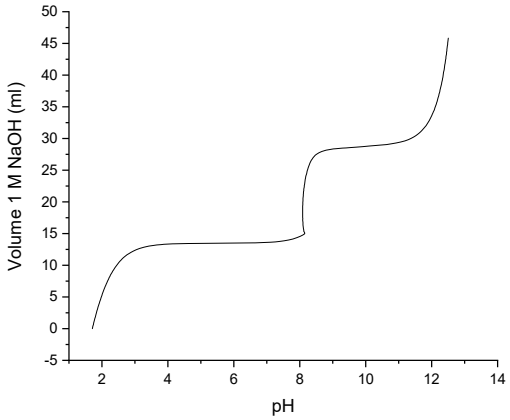

Figure 5.9: Titration curve of 50 ml 15.6 mM tertiary NDI in water by addition of 1 M sodium hydroxide.

5.2.1 NMR Characterization of NDI

The equilibrium constant for the dimerization of NDI in pH 7 phosphate buffer in D_2O was acquired by measuring ^{1}H-NMR spectra at the concentrations shown in Figure 5.10. Although an equilibrium constant for the dimerization of NDI in water has been reported, values for the sodium phosphate buffer electrolyte used in this work do not exist.

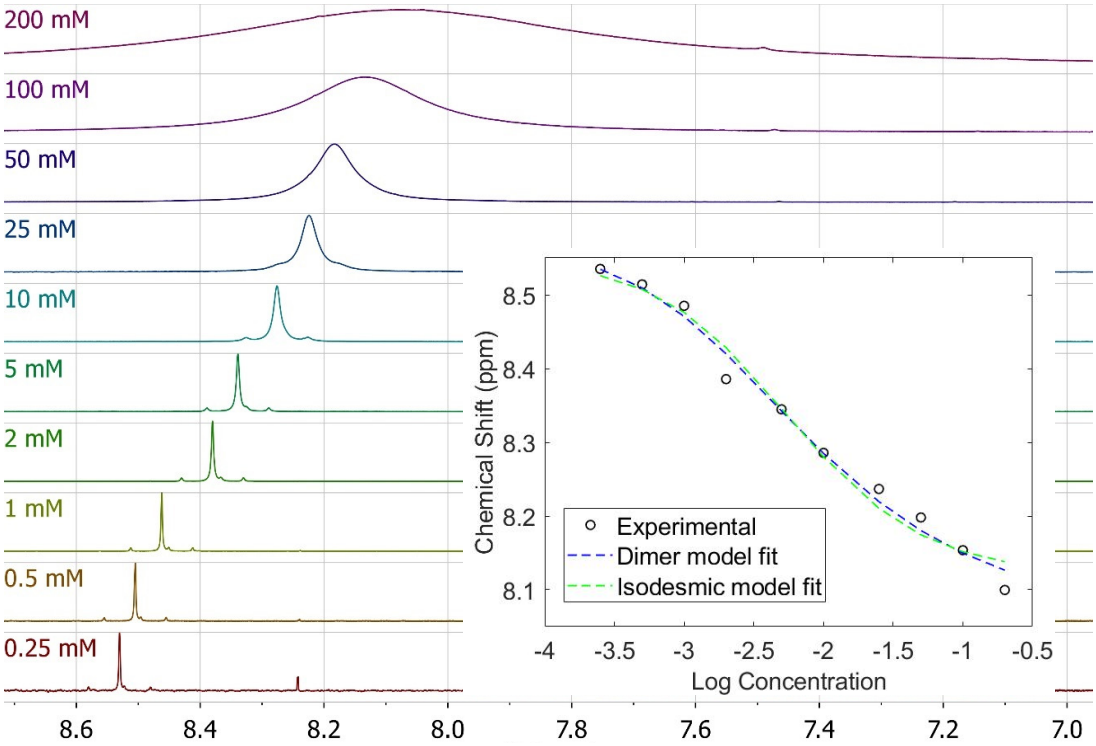

Figure 5.10: Self-association study of NDI in pH 7 phosphate buffer solution in D_2O. The x-axis shows the chemical shift in ppm. The inset figure shows the fitting of the shifts to the dimer and isodesmic models.

The peaks are seen to move towards lower chemical shifts, as well as broaden at higher concentrations. The peak broadening is indicative of self-association,[58, 65] and made measurements at higher concentrations than 400 mM impossible. The model fits shown in the inset of Figure 5.10 yielded equilibrium constants of K=146 M^{-1} with a residual of 0.01 ppm for the dimer model and K = 104 M^{-1} with a residual of 0.04 ppm for the isodesmic model.

Diffusion coefficients measured and calculated by diffusion NMR will, for a self-associative system, have the following relationship:

$$D_{measured} = xD_{monomer} + (1 - x)D_{dimer}, \qquad 9$$

Where x is the molar fraction of monomer in solution and D is the diffusion coefficient. In order to determine the diffusion coefficients for the monomer and the dimer, diffusion coefficients were collected for a range of concentrations, shown in Table 5.2. Furthermore, the sodium salt of a molecule commonly used as an NMR reference, 3-(trimethylsilyl)propionic-2,2,3,3-d4 acid (TSP-D4) was added to the stock solution from which the samples were prepared. Thus, although it had a constant concentration in all samples the diffusion coefficient of TSP-D4 was seen to decrease with increasing concentration of NDI due to the increased viscosity of the solution. This allowed the diffusion coefficients of NDI to be normalized against that of the reference molecule, negating the bias from viscosity.

Table 5.2: Diffusion coefficients measured by diffusion NMR.

C (mM)	D (cm²/s)	D ref (cm²/s)	x	D_{dimer} (cm²/s)	$D_{monomer}$ (cm²/s)
0.25	2.4(1) x 10-6	4.5(1) x 10-6	0.94		
1	2.3(0) x 10-6	4.6(1) x 10-6	0.81	1.8(1) x 10-6	2.5(1) x 10-6
5	2.2(1) x 10-6	4.5(0) x 10-6	0.55		
10	2(1) x 10-6	4.5(0) x 10-6	0.44		
25	1.9(2) x 10-6	4.6(3) x 10-6	0.31	1.8(1) x 10-6	2.5(1) x 10-6
50	1.8(1) x 10-6	4(4) x 10-6	0.23	1.6(1) x 10-6	2.2(1) x 10-6
100	1.6(2) x 10-6	3.4(1) x 10-6	0.17		
200	1.4(1) x 10-6	3.6(2) x 10-6	0.12		
400	1(0) x 10-6	2.5(1) x 10-6	0.10		

Inserting the above parameters into Equation 9 resulted in an overdetermined system of equations which was solved computationally by QR-factorization using column pivoting. The diffusion coefficients for the monomer and the dimer were calculated for the concentrations analyzed using RDE and are shown in Table 5.2.

5.2.2 Electrochemistry

The electrochemistry of NDI was examined by CV at a range of different pH values, to gain understanding of the electron transfer reaction mechanism. Figure 5.11a and Figure 5.11b show CVs for NDI at pH 0 and 7 respectively. D e to the broadness of the peak at pH 0 and the occurrence of two separate redox couples at pH 7, it is concluded that the reduction involves more than one electron. Later in this section, by combining information from rotating disk electrode (RDE) voltammetry and the potential – pH diagram, it is established that both electrolytes have redox-processes that involve a total of two electrons. Therefore, the broadness of the first reduction at pH 7, which might typically indicate two or more reductions taking place at the same time, is hard to explain.

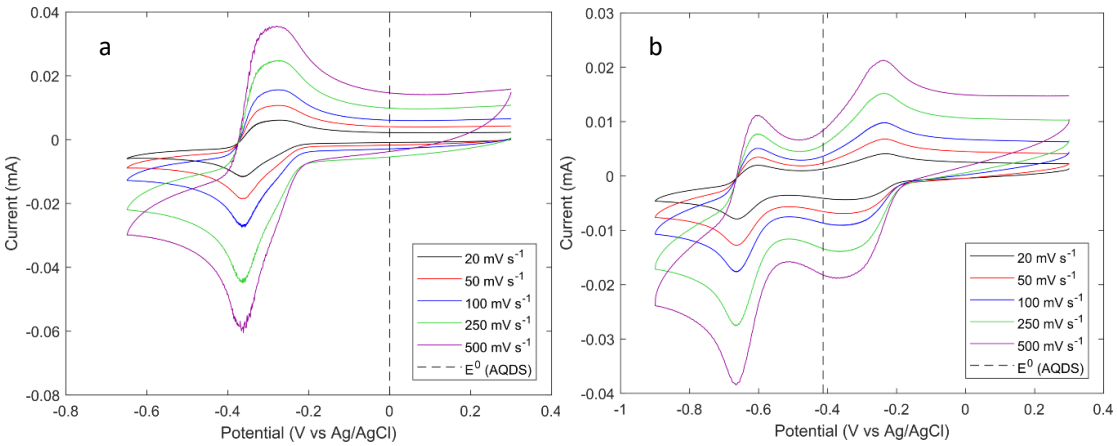

Figure 5.11: CVs for 1 mM NDI in a) 1 M H_2SO_4 and b) neutral phosphate buffer. The dashed vertical line illustrates the reduction potential of AQDS, as comparison.

A plot of the reduction potentials for NDI at different pHs is seen in Figure 5.12. The red diamonds show that the first reduction potential is independent of pH and does not involve any protons. The

second reduction, the blue markers in the figure, has a slope of 91 mV/pH unit at pH below 3, indicating a one electron-1.5 proton relationship, according to Equation 4.

It should be remarked that the reduction of NDI occurs at far negative potentials, and if used in a redox flow battery, it would possibly yield an operating voltage among the highest of the previously reported structures in aqueous solutions.[18, 31, 34, 40, 66-71] Indeed, more negative potentials are not beneficial, due to the parasitic HER reactions eventually taking precedence.

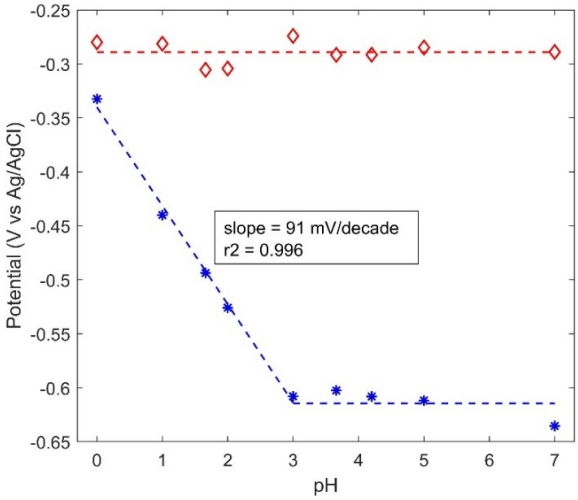

Figure 5.12: Potential-pH diagram of NDI. At pH below 3, the second reduction follows a one electron-1.5 proton slope (or 2 electrons and three protons), and at higher pHs, it is independent of pH, as the first reduction couple is over the whole range.

Similar to the procedure done for AQDS, RDE was coupled with diffusion NMR to assess the accessible concentration of NDI in a neutral buffered solution and tested whether it corresponded to dimerization. The acid The diffusion coefficients from diffusion NMR were found to be 2.57 and 2.34 x 10^{-6} cm^2 s^{-1} for the acid and neutral solutions respectively. From the slope in Figure 5.13, the accessible concentration was calculated, through the Levich equation, and showed that the reduction of 1 mM NDI at pH 0 only involves two electrons. Addition of three protons to each NDI molecule at pH values as high as 3 is unlikely, since the third proton would be at a weakly basic carbonyl or imide nitrogen. This is further supported by the lack of buffering at lower pHs in the titration curve in Figure 5.9.

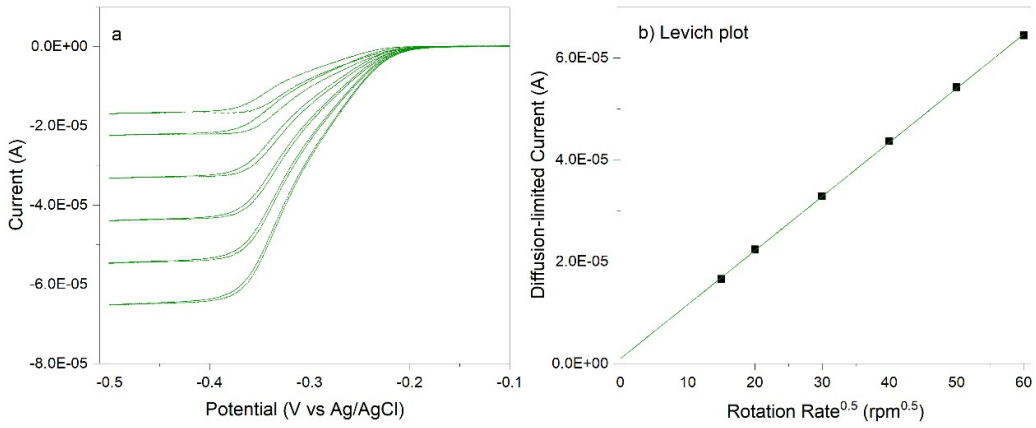

Figure 5.13: RDE analysis for 1 mM NDI in 1 M H_2SO_4.

Based on this relationship and reasoning, the reduction scheme in Figure 5.14 is proposed for acidic solutions as follows.

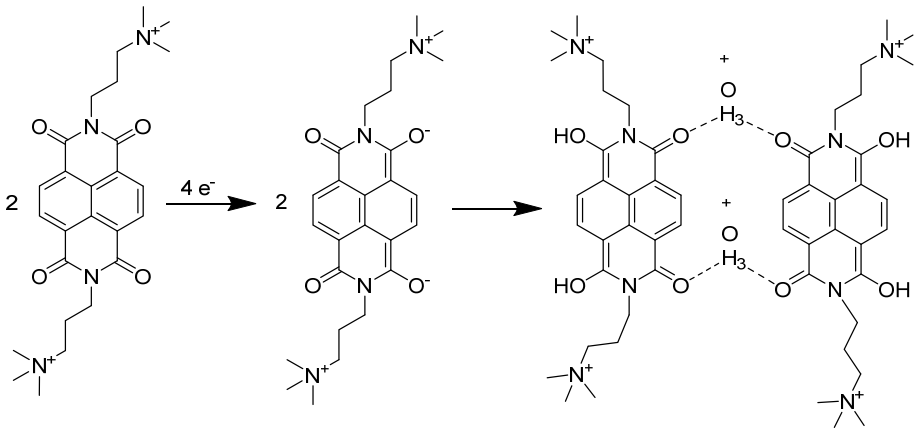

Figure 5.14: The proposed reduction mechanism for NDI in acidic solutions at pH values lower than 3.

5.2.3 Dimerization

After the work on AQDS which showed the impact of dimerization on its electrochemical properties, it would be imprudent to neglect examining whether the same behavior could be seen for NDI.

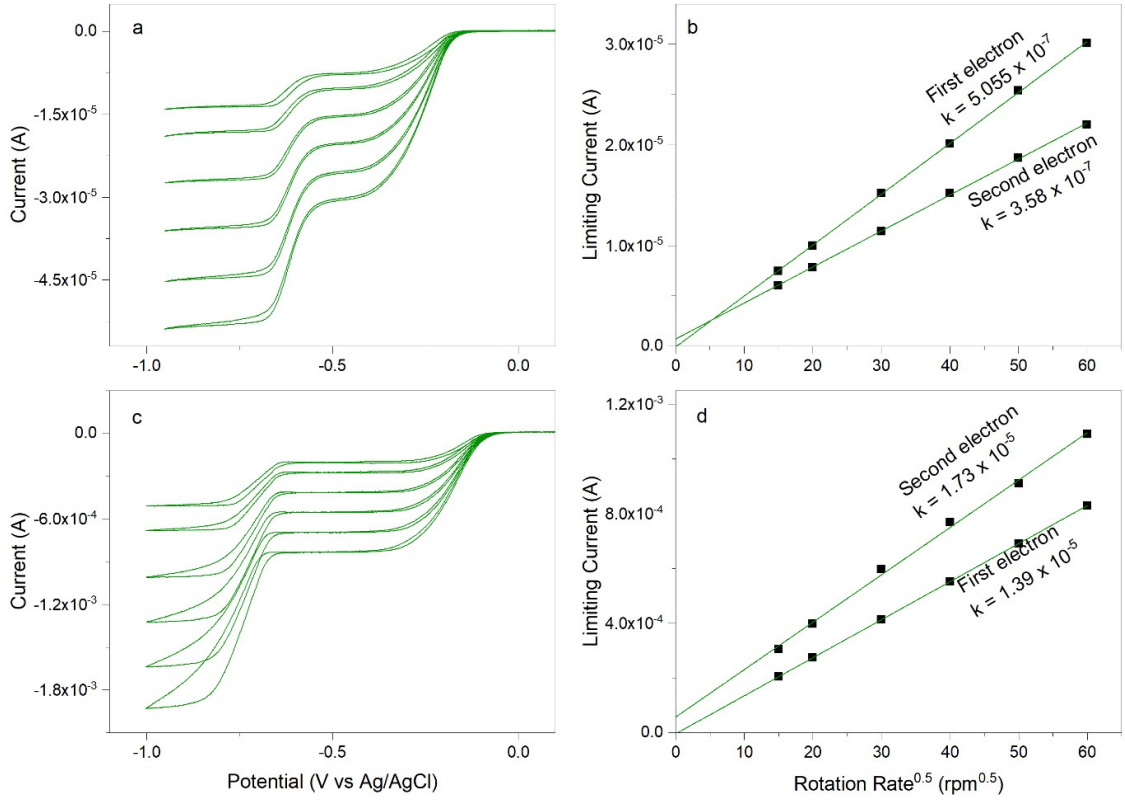

Figure 5.15: RDE analysis for NDI in pH 7 phosphate buffer solution at concentrations of a), b) 1 mM and c), d) 50 mM.

Figure 5.15 shows the results from RDE measurements of NDI in neutral buffered solution. Two well-defined diffusion-limited current plateaus were observed, with the first reduction coming at a less

negative potential, and the second reduction at a more negative potential, for 50 mM compared to 1 mM. The large distance between reduction potentials could enable the use of NDI in a symmetric flow battery, where NDI is utilized as both cathodic and anodic electrolytes simultaneously but is not further examined in this work. Furthermore, the Levich slope for the first electron is steeper than for the second electron at 1 mM, whereas the opposite is true for 50 mM. This suggests a CE-mechanism for the second electron, where a possible reaction could be the dissociation of the dimer. Further support of a CE-mechanism is that the line of the Levich plot for the second electron does not quite pass through zero, as well it having slightly parabolic shape, more clearly seen for the 50 mM sample. However, for analyzing the limiting currents of the first electron reduction in the system that contains a mixture of monomer and dimer, the following modified Levich expression was used:

$$i_l \omega^{-\frac{1}{2}} = 0.201 F A_{rde} (n_m C_m D_m^{\frac{2}{3}} + n_d C_d D_d^{\frac{2}{3}}) \nu^{-\frac{1}{6}}, \qquad 10$$

Where the indices m and d denote the monomer and dimer respectively. Due to the seemingly more complex nature of the transfer of the second electron, only the limiting currents from the first plateau were used in the following analysis.

By entering the diffusion coefficients for the monomer and dimer which were calculated in the previous section, along with the concentrations corresponding to the equilibrium constant of K=146 M^{-1}, it is possible to determine the number of electrons accessible for reduction of the dimer.

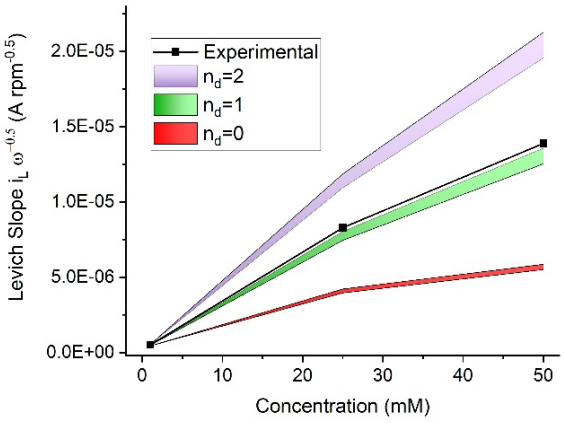

Figure 5.16: Comparison of Levich slopes for different number of electrons given for the first electron reduction of NDI in pH 7 phosphate buffer. The black line shows the values acquired experimentally with RDE.

Figure 5.16 shows the Levich slopes for three different values for n_{dimer}. The scenario where the dimer can gain one electron – half as much as the monomer – is clearly the one in closest agreement with experimental data. The green area lies slightly below the experimental values, likely due to the inaccuracy of the equilibrium constant acquired by NMR. To examine whether this error is large enough to bring uncertainty to the above conclusion, the same analysis as above was repeated, but with equilibrium constants of 40 M^{-1} and 400 M^{-1} instead.

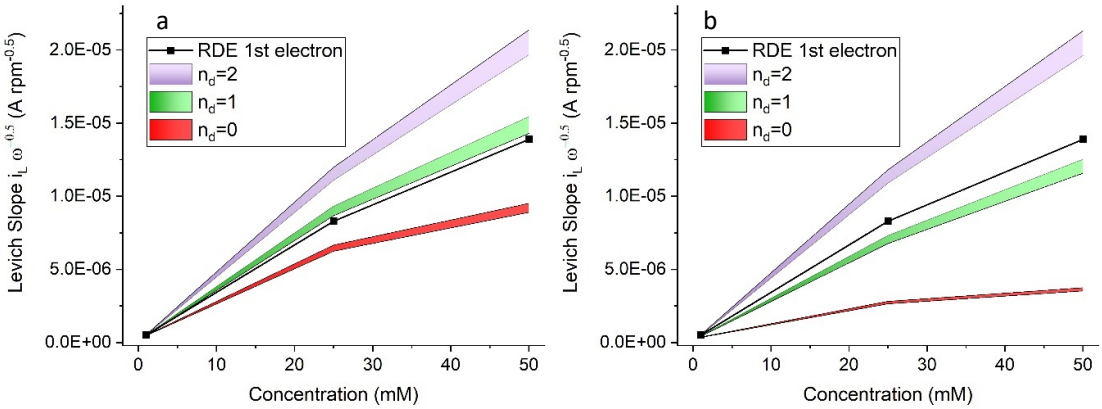

Figure 5.17: Levich slope comparisons based on a) K = 40 M^{-1} and b) K = 400 M^{-1}.

Figure 5.17 shows that even if the equilibrium constant of 146 M^{-1} is was to shift by a rough factor three in either direction, the conclusion would unambiguously be the same.

5.2.4 Bulk Electrolysis

A solution of 25 mM NDI in pH 6.4 sodium phosphate buffer was cycled in a bulk electrolysis cell, where all of the material is reduced, as opposed to CV and RDE, where only a small fraction of the material is probed. Two plateaus were seen at the electrolysis, corresponding to the two separate redox couples, illustrated by the overlaid CV in Figure 4.14.

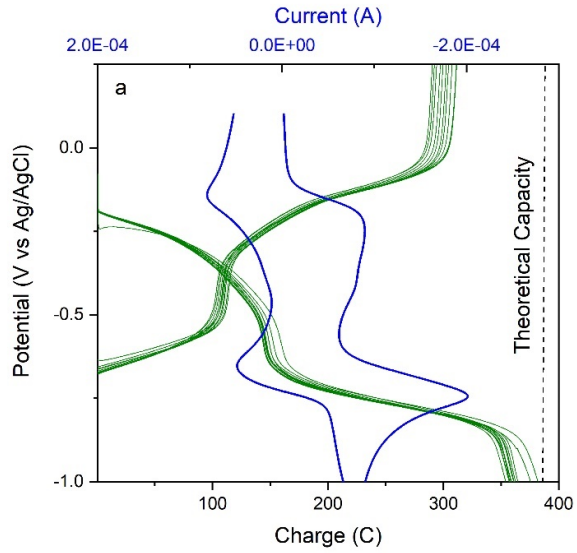

Figure 5.18: Bulk electrolysis sweep of 25 mM NDI in pH 6.4 sodium phosphate buffer solution. A CV is overlaid, to illustrate the relationship between the two electrons and the two potential plateaus. b) CVs collected every 20 minutes during the bulk electrolysis.

The reductive capacities reach values close to the theoretical capacity depicted by the dashed black line, see Figure 5.18. A possible explanation to why NDI is quantitatively reduced with BE in galvanostatic mode, and AQDS is not, is that the dissociation of the NDI dimer proceeds more rapidly.

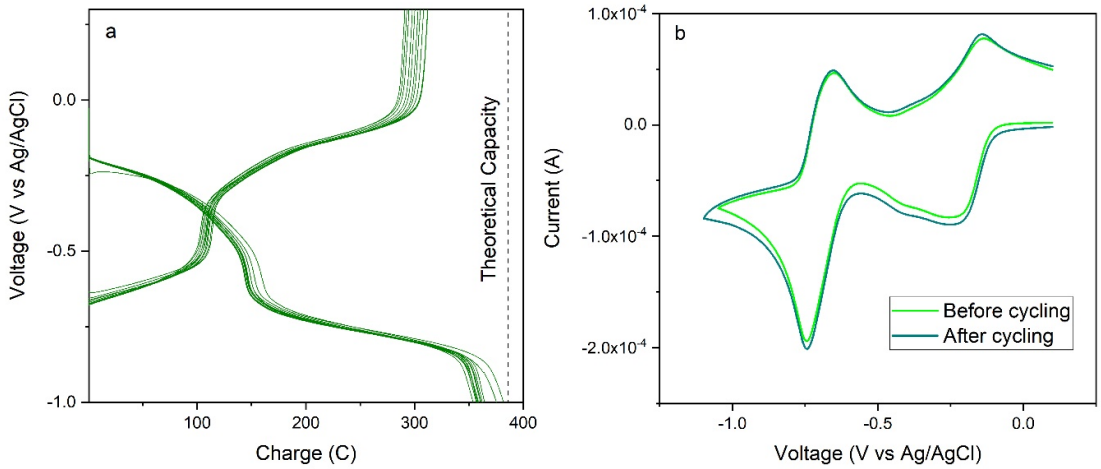

Figure 5.19: a) Bulk electrolysis of 25 mM NDI in pH 6.4 sodium phosphate buffer. b) CVs collected before and after reducing and oxidizing the electrolyte for 12 cycles.

Continuous cycling at a current of 15 mA was performed for twelve cycles whereupon A CV was collected, roughly a week after starting. The CV was compared to the initial, untouched solution, and it was seen that they overlapped perfectly, indicating little or no material degradation over the course of the experiment, showing the exceptional stability of NDI.

6 Comparison Between NDI and AQDS

While both AQDS and NDI dimerize in solution, and both suffer some form or electrochemical impediment due to the dimerization, large differences exist in their chemical and electrochemical behavior. The reduction of both molecules involves two electrons, but for NDI, the reduction potential for the first electron is pH independent, resulting in a tunable potential gap between the first and the second electron. The diffusion coefficient for NDI is slightly lower than for AQDS, which might decrease the power density somewhat, for a given flow rate. On the other hand, the larger size of NDI will decrease the permeability of the molecule through the membrane separating it from the side containing the positive electrolyte, resulting in a lower capacity fade with time. Lastly, the dimerization of NDI, while happening to a much larger extent than for AQDS, does not limit the accessible capacity from bulk electrolysis as it does for AQDS. The reason for this is yet unclear, but if the reason is simply that the respective inactive dimers need time to dissociate in response of the shifting equilibrium due to the consumption of monomer, then this is might not be a big problem for either molecule in the application of large-scale flow batteries, as the charge and discharge times are longer than for most lab-scale flow battery experiments.

7 Conclusions and Future Work

The dimerization of AQDS, NDI and other planar aromatic molecules is indeed a phenomenon that needs to be taken into account when considering the viability of organic molecules for AqORFBs. Already at concentrations of 50 mM, a considerable decrease of capacity was seen for AQDS. This is detrimental for practical applications as AqORFBs since a typical operating concentration for the final application is 10-20 times higher.[12, 33] Although NDI has yet to be examined in a flow cell at high concentrations, there are indications that the dimerization will not be as problematic for NDI as for AQDS. Thus, by employing a deeper electrochemical analysis of the molecules, a considerable amount of information about their respective applicability for flow batteries could be gleaned, as was envisioned in Section 2.

It is further concluded that NDI shows great promise as a negative electrolyte material, due to its ease of synthesis, deeply negative reduction potential and exceptional stability. This gives credence to the synthesis strategy stated in Section 2, to solubilize and examine candidate molecules currently used in non-aqueous flow batteries as well as other related non-aqueous applications.

Lastly, in pursuit of novel materials for aqueous organic flow batteries, one interesting synthesis strategy is simply to solubilize promising candidates from non-aqueous flow batteries and examine their behavior in aqueous electrolytes.

Future work includes looking into the apparent rate constant of the electron transfer of NDI, which is an important figure of merit as it partly determines the overpotential and thus the energy efficiency of the system. To tune the reduction potential of NDI, adding electron withdrawing and electron donating substituents to the naphthalene core will tested. The molecule needs to be tested in an actual flow battery, where it can be investigated how effects such as crossover, diffusivity and kinetics influence its performance. Furthermore, the possibility of using NDI as a molecule for symmetric flow batteries should be pursued, as there are great advantages in terms of crossover and mass-production scalability to be had, if the same molecule can be used on both the negative and the positive side of the battery.

References

[1] J. Zachos, M. Pagani, L. Sloan, E. Thomas, K. Billups, Trends, Rhythms, and Aberrations in Global Climate 65 Ma to Present, Science, 292 (2001) 686-693,
[2] L.A. Frakes, J.E. Francis, J.I. Syktus, Climate Modes of the Phanerozoic, Cambridge University Press, Cambridge, 1992.
[3] J. Tyndall, XXVII. On radiation through the earth's atmosphere, The London, Edinburgh, and Dublin Philosophical Magazine and Journal of Science, 25 (1863) 200-206, https://doi.org/10.1080/14786446308643443.
[4] G. Hartfield, J. Blunden, D.S. Arndt, State of the Climate in 2017, Bulletin of the American Meteorological Society, 99 (2018) Si-S310, https://doi.org/10.1175/2018BAMSStateoftheClimate.1.
[5] P.K. Tans, Ralph, CO2 data from Mauna Loa, 2018,
[6] C. MacFarling Meure, D. Etheridge, C. Trudinger, P. Steele, R. Langenfelds, T. van Ommen, A. Smith, J. Elkins, Law Dome CO2, CH4 and N2O ice core records extended to 2000 years BP, 33 (2006), https://doi.org/10.1029/2006GL026152.
[7] D.M. Etheridge, L.P. Steele, R.L. Langenfelds, R.J. Francey, J.-M. Barnola, V.I. Morgan, Natural and anthropogenic changes in atmospheric CO2 over the last 1000 years from air in Antarctic ice and firn, 101 (1996) 4115-4128, https://doi.org/10.1029/95JD03410.
[8] NASA's Goddard Institute for Space Studies (GISS), 2018,
[9] Renewable Energy Policy Network for the 21st Century (REN21), (2018),
[10] M.G.K. Izumi, Trends 2018 in Photovoltaic Applications, IEA International Energy Agency, 2018,
[11] Annual Market Update 2017 - Global Wind Report, Global Wind Energy Council, 2017,
[12] R.M. Darling, K.G. Gallagher, J.A. Kowalski, S. Ha, F.R. Brushett, Pathways to low-cost electrochemical energy storage: a comparison of aqueous and nonaqueous flow batteries, Energy Environ. Sci., 7 (2014) 3459-3477, https://doi.org/10.1039/c4ee02158d.
[13] M.B.C. Salles, T.N. Gadotti, M.J. Aziz, W.W. Hogan, Potential revenue and breakeven of energy storage systems in PJM energy markets, Environ Sci Pollut Res Int, (2018), https://doi.org/10.1007/s11356-018-3395-y.
[14] A.A. Solomon, D. Bogdanov, C. Breyer, Curtailment-storage-penetration nexus in the energy transition, Applied Energy, 235 (2019) 1351-1368, https://doi.org/10.1016/j.apenergy.2018.11.069.
[15] A. Narayanan, K. Mets, M. Strobbe, C. Develder, Feasibility of 100% renewable energy-based electricity production for cities with storage and flexibility, Renewable Energy, 134 (2019) 698-709, https://doi.org/10.1016/j.renene.2018.11.049.
[16] A.Z. Weber, M.M. Mench, J.P. Meyers, P.N. Ross, J.T. Gostick, Q. Liu, Redox flow batteries: a review, J. Appl. Electrochem., 41 (2011) 1137-1164, https://doi.org/10.1007/s10800-011-0348-2.
[17] M. Rychcik, M. Skyllas-Kazacos, Characteristics of a new all-vanadium redox flow battery, J. Power Sources, 22 (1988) 59-67, https://doi.org/10.1016/0378-7753(88)80005-3.
[18] B. Huskinson, M.P. Marshak, C. Suh, S. Er, M.R. Gerhardt, C.J. Galvin, X. Chen, A. Aspuru-Guzik, R.G. Gordon, M.J. Aziz, A metal-free organic-inorganic aqueous flow battery, Nature, 505 (2014) 195-198, https://doi.org/10.1038/nature12909.
[19] C. Minke, U. Kunz, T. Turek, Carbon felt and carbon fiber - A techno-economic assessment of felt electrodes for redox flow battery applications, J. Power Sources, 342 (2017) 116-124, https://doi.org/10.1016/j.jpowsour.2016.12.039.
[20] W. Wang, Q. Luo, B. Li, X. Wei, L. Li, Z. Yang, Recent Progress in Redox Flow Battery Research and Development, 23 (2013) 970-986, https://doi.org/10.1002/adfm.201200694.
[21] S. Maurya, S.-H. Shin, Y. Kim, S.-H. Moon, A review on recent developments of anion exchange membranes for fuel cells and redox flow batteries, RSC Advances, 5 (2015) 37206-37230, https://doi.org/10.1039/c5ra04741b.
[22] Z. Yuan, H. Zhang, X. Li, Ion conducting membranes for aqueous flow battery systems, Chem Commun (Camb), 54 (2018) 7570-7588, https://doi.org/10.1039/c8cc03058h.

[23] R. Ye, D. Henkensmeier, S.J. Yoon, Z. Huang, D.K. Kim, Z. Chang, S. Kim, R. Chen, Redox Flow Batteries for Energy Storage: A Technology Review, Journal of Electrochemical Energy Conversion and Storage, 15 (2017) 010801, https://doi.org/10.1115/1.4037248.
[24] J. Xu, H.R. Thomas, R.W. Francis, K.R. Lum, J. Wang, B. Liang, A review of processes and technologies for the recycling of lithium-ion secondary batteries, J. Power Sources, 177 (2008) 512-527, https://doi.org/10.1016/j.jpowsour.2007.11.074.
[25] J. Ordoñez, E.J. Gago, A. Girard, Processes and technologies for the recycling and recovery of spent lithium-ion batteries, Renewable and Sustainable Energy Reviews, 60 (2016) 195-205, https://doi.org/10.1016/j.rser.2015.12.363.
[26] G.E. Blomgren, The development and future of lithium ion batteries, J. Electrochem. Soc., 164 (2017) A5019-A5025, https://doi.org/10.1149/2.0251701jes.
[27] H.D. Doughty, Vehicle Battery Safety Roadmap Guidance, National Renewable Energy Laboratory, 2012,
[28] M.C. Wu, T.S. Zhao, H.R. Jiang, Y.K. Zeng, Y.X. Ren, High-performance zinc bromine flow battery via improved design of electrolyte and electrode, J. Power Sources, 355 (2017) 62-68, https://doi.org/10.1016/j.jpowsour.2017.04.058.
[29] M. Zheng, J. Sun, C.J. Meinrenken, T. Wang, Pathways Toward Enhanced Techno-Economic Performance of Flow Battery Systems in Energy System Applications, Journal of Electrochemical Energy Conversion and Storage, 16 (2018) 021001-021001-021011, https://doi.org/10.1115/1.4040921.
[30] M. Zhang, M. Moore, J.S. Watson, T.A. Zawodzinski, R.M. Counce, Capital Cost Sensitivity Analysis of an All-Vanadium Redox-Flow Battery, J. Electrochem. Soc., 159 (2012) A1183-A1188, https://doi.org/10.1149/2.041208jes.
[31] P. Leung, A.A. Shah, L. Sanz, C. Flox, J.R. Morante, Q. Xu, M.R. Mohamed, C. Ponce de León, F.C. Walsh, Recent developments in organic redox flow batteries: A critical review, J. Power Sources, 360 (2017) 243-283, https://doi.org/10.1016/j.jpowsour.2017.05.057.
[32] F. Pan, Q. Wang, Redox Species of Redox Flow Batteries: A Review, Molecules, 20 (2015) 20499-20517, https://doi.org/10.3390/molecules201119711.
[33] R. Dmello, J.D. Milshtein, F.R. Brushett, K.C. Smith, Cost-driven materials selection criteria for redox flow battery electrolytes, J. Power Sources, 330 (2016) 261-272, https://doi.org/10.1016/j.jpowsour.2016.08.129.
[34] T. Janoschka, N. Martin, U. Martin, C. Friebe, S. Morgenstern, H. Hiller, M.D. Hager, U.S. Schubert, An aqueous, polymer-based redox-flow battery using non-corrosive, safe, and low-cost materials, Nature, 527 (2015) 78-81, https://doi.org/10.1038/nature15746.
[35] X. Wei, W. Pan, W. Duan, A. Hollas, Z. Yang, B. Li, Z. Nie, J. Liu, D. Reed, W. Wang, V. Sprenkle, Materials and Systems for Organic Redox Flow Batteries: Status and Challenges, ACS Energy Letters, 2 (2017) 2187-2204, https://doi.org/10.1021/acsenergylett.7b00650.
[36] K. Wedege, E. Drazevic, D. Konya, A. Bentien, Organic Redox Species in Aqueous Flow Batteries: Redox Potentials, Chemical Stability and Solubility, Sci Rep, 6 (2016) 39101, https://doi.org/10.1038/srep39101.
[37] S. Er, C. Suh, M.P. Marshak, A. Aspuru-Guzik, Computational design of molecules for an all-quinone redox flow battery, Chem Sci, 6 (2015) 885-893, https://doi.org/10.1039/c4sc03030c.
[38] M.R. Gerhardt, L. Tong, R. Gómez-Bombarelli, Q. Chen, M.P. Marshak, C.J. Galvin, A. Aspuru-Guzik, R.G. Gordon, M.J. Aziz, Anthraquinone Derivatives in Aqueous Flow Batteries, Advanced Energy Materials, 7 (2017) 1601488, https://doi.org/10.1002/aenm.201601488.
[39] W. Liu, W. Lu, H. Zhang, X. Li, Aqueous Flow Batteries: Research and Development, Chemistry – A European Journal, (2018), https://doi.org/10.1002/chem.201802798.
[40] S.D. Pineda Flores, G.C. Martin-Noble, R.L. Phillips, J. Schrier, Bio-Inspired Electroactive Organic Molecules for Aqueous Redox Flow Batteries. 1. Thiophenoquinones, The Journal of Physical Chemistry C, 119 (2015) 21800-21809, https://doi.org/10.1021/acs.jpcc.5b05346.

[41] D.G. Kwabi, K. Lin, Y. Ji, E.F. Kerr, M.-A. Goulet, D. De Porcellinis, D.P. Tabor, D.A. Pollack, A. Aspuru-Guzik, R.G. Gordon, M.J. Aziz, Alkaline Quinone Flow Battery with Long Lifetime at pH 12, Joule, 2 (2018) 1894-1906, https://doi.org/10.1016/j.joule.2018.07.005.
[42] J.A. Kowalski, L. Su, J.D. Milshtein, F.R. Brushett, Recent advances in molecular engineering of redox active organic molecules for nonaqueous flow batteries, Current Opinion in Chemical Engineering, 13 (2016) 45-52, https://doi.org/10.1016/j.coche.2016.08.002.
[43] J.D. Milshtein, A.P. Kaur, M.D. Casselman, J.A. Kowalski, S. Modekrutti, P.L. Zhang, N. Harsha Attanayake, C.F. Elliott, S.R. Parkin, C. Risko, F.R. Brushett, S.A. Odom, High current density, long duration cycling of soluble organic active species for non-aqueous redox flow batteries, Energy & Environmental Science, 9 (2016) 3531-3543, https://doi.org/10.1039/c6ee02027e.
[44] T.J. Carney, S.J. Collins, J.S. Moore, F.R. Brushett, Concentration-Dependent Dimerization of Anthraquinone Disulfonic Acid and Its Impact on Charge Storage, Chem. Mater., 29 (2017) 4801-4810, https://doi.org/10.1021/acs.chemmater.7b00616.
[45] H. Yan, Z. Chen, Y. Zheng, C. Newman, J.R. Quinn, F. Dotz, M. Kastler, A. Facchetti, A high-mobility electron-transporting polymer for printed transistors, Nature, 457 (2009) 679-686, https://doi.org/10.1038/nature07727.
[46] N. Zhou, A. Facchetti, Naphthalenediimide (NDI) polymers for all-polymer photovoltaics, Mater. Today, 21 (2018) 377-390, https://doi.org/10.1016/j.mattod.2018.02.003.
[47] N. Elgrishi, K.J. Rountree, B.D. McCarthy, E.S. Rountree, T.T. Eisenhart, J.L. Dempsey, A Practical Beginner's Guide to Cyclic Voltammetry, J. Chem. Educ., 95 (2017) 197-206, https://doi.org/10.1021/acs.jchemed.7b00361.
[48] J.I. Goldsmith, K. Takada, H.D. Abruna, Probing diffusional transport in redox-active dendrimers, J. Phys. Chem. B, 106 (2002) 8504-8513, https://doi.org/10.1021/jp014080k.
[49] E. Tourwé, T. Breugelmans, R. Pintelon, A. Hubin, Extraction of a quantitative reaction mechanism from linear sweep voltammograms obtained on a rotating disk electrode. Part II: Application to the redoxcouple, J. Electroanal. Chem., 609 (2007) 1-7, https://doi.org/10.1016/j.jelechem.2006.12.019.
[50] F. Scholz, A.M. Bond, Electroanalytical methods : guide to experiments and applications, 2nd, rev. and extended ed., Springer, Heidelberg ; New York, 2010.
[51] A.J. Bard, L.R. Faulkner, Electrochemical methods : fundamentals and applications, 2nd ed., Wiley, New York, 2001.
[52] P. Zanello, Royal Society of Chemistry (Great Britain), Inorganic electrochemistry : theory, practice and applications, Royal Society of Chemistry, Cambridge, 2003.
[53] R.G. Compton, C.E. Banks, Understanding voltammetry, Third edition. ed., World Scientific, New Jersey, 2018.
[54] M. Quan, D. Sanchez, M.F. Wasylkiw, D.K. Smith, Voltammetry of Quinones in Unbuffered Aqueous Solution: Reassessing the Roles of Proton Transfer and Hydrogen Bonding in the Aqueous Electrochemistry of Quinones, J. Am. Chem. Soc., 129 (2007) 12847-12856, https://doi.org/10.1021/ja0743083.
[55] C. Batchelor-McAuley, Q. Li, S.M. Dapin, R.G. Compton, Voltammetric characterization of DNA intercalators across the full pH range: anthraquinone-2,6-disulfonate and anthraquinone-2-sulfonate, J. Phys. Chem. B, 114 (2010) 4094-4100, https://doi.org/10.1021/jp1008187.
[56] M. Seralathan, S.K. Rangarajan, Scheme of squares: Part I. Systems formalism for potentiostatic studies, Journal of Electroanalytical Chemistry and Interfacial Electrochemistry, 191 (1985) 209-228, https://doi.org/https://doi.org/10.1016/S0022-0728(85)80018-8.
[57] W.S. Price, Pulsed-field gradient nuclear magnetic resonance as a tool for studying translational diffusion: Part 1. Basic theory, Concepts in Magnetic Resonance, 9 (1997) 299-336, https://doi.org/10.1002/(SICI)1099-0534(1997)9:5<299::AID-CMR2>3.0.CO;2-U.
[58] D.P. Frueh, Practical aspects of NMR signal assignment in larger and challenging proteins, Prog. Nucl. Magn. Reson. Spectrosc., 78 (2014) 47-75, https://doi.org/10.1016/j.pnmrs.2013.12.001.
[59] M.S. Cubberley, B.L. Iverson, 1H NMR Investigation of Solvent Effects in Aromatic Stacking Interactions, J. Am. Chem. Soc., 123 (2001) 7560-7563, https://doi.org/10.1021/ja015817m.

[60] A.D. Bain, Chemical Exchange Effects in NMR, in: J.C. Lindon (Ed.) Encyclopedia of Spectroscopy and Spectrometry, Elsevier, Oxford, 1999, pp. 198-207.
[61] J.S. Chen, R.B. Shirts, Iterative determination of the NMR monomer shift and dimerization constant in a self-associating system, The Journal of Physical Chemistry, 89 (1985) 1643-1646, https://doi.org/10.1021/j100255a018.
[62] M.T. McDermott, K. Kneten, R.L. McCreery, Anthraquinonedisulfonate adsorption, electron-transfer kinetics, and capacitance on ordered graphite electrodes: the important role of surface defects, The Journal of Physical Chemistry, 96 (1992) 3124-3130, https://doi.org/10.1021/j100186a063.
[63] R.J. Forster, J.P. O'Kelly, Protonation reactions of anthraquinone-2,7-disulphonic acid in solution and within monolayers, J. Electroanal. Chem., 498 (2001) 127-135, https://doi.org/10.1016/s0022-0728(00)00331-4.
[64] C. Sissi, L. Lucatello, A. Paul Krapcho, D.J. Maloney, M.B. Boxer, M.V. Camarasa, G. Pezzoni, E. Menta, M. Palumbo, Tri-, tetra- and heptacyclic perylene analogues as new potential antineoplastic agents based on DNA telomerase inhibition, Bioorg. Med. Chem., 15 (2007) 555-562, https://doi.org/10.1016/j.bmc.2006.09.029.
[65] A.T. Alexandrescu, K. Rathgeb-Szabo, An NMR investigation of solution aggregation reactions preceding the misassembly of acid-denatured cold shock protein A into fibrils11Edited by P. E. Wright, J. Mol. Biol., 291 (1999) 1191-1206, https://doi.org/10.1006/jmbi.1999.3039.
[66] K. Lin, Q. Chen, M.R. Gerhardt, L. Tong, S.B. Kim, L. Eisenach, A.W. Valle, D. Hardee, R.G. Gordon, M.J. Aziz, M.P. Marshak, Alkaline quinone flow battery, Science, 349 (2015) 1529-1532, https://doi.org/10.1126/science.aab3033.
[67] T. Janoschka, C. Friebe, M.D. Hager, N. Martin, U.S. Schubert, An Approach Toward Replacing Vanadium: A Single Organic Molecule for the Anode and Cathode of an Aqueous Redox-Flow Battery, ChemistryOpen, 6 (2017) 216-220, https://doi.org/10.1002/open.201600155.
[68] A. Orita, M.G. Verde, M. Sakai, Y.S. Meng, A biomimetic redox flow battery based on flavin mononucleotide, Nat Commun, 7 (2016) 13230, https://doi.org/10.1038/ncomms13230.
[69] C. DeBruler, B. Hu, J. Moss, X. Liu, J. Luo, Y. Sun, T.L. Liu, Designer Two-Electron Storage Viologen Anolyte Materials for Neutral Aqueous Organic Redox Flow Batteries, Chem, 3 (2017) 961-978, https://doi.org/10.1016/j.chempr.2017.11.001.
[70] B. Yang, L. Hoober-Burkhardt, F. Wang, G.K. Surya Prakash, S.R. Narayanan, An Inexpensive Aqueous Flow Battery for Large-Scale Electrical Energy Storage Based on Water-Soluble Organic Redox Couples, J. Electrochem. Soc., 161 (2014) A1371-A1380, https://doi.org/10.1149/2.1001409jes.
[71] J. Luo, B. Hu, C. Debruler, T.L. Liu, A pi-Conjugation Extended Viologen as a Two-Electron Storage Anolyte for Total Organic Aqueous Redox Flow Batteries, Angew. Chem. Int. Ed. Engl., 57 (2018) 231-235, https://doi.org/10.1002/anie.201710517.